



Quantum AI and hybrid simulators for a Universal Quantum Field Computation Model



Philip Baback Alipour*, Thomas Aaron Gulliver

Department of Electrical and Computer Engineering, University of Victoria, Victoria BC, V8W 2Y2, Canada

REVIEW HIGHLIGHTS

- Review of notable quantum simulation methods used in simulating QFTs and other related sciences.
- Review model strengths and limitations by its common measurement parameters in predicting states.
- Propose a universal QFCM to make strong predictions of system states via QAI methods.

ARTICLE INFO

Method name:

Universal Quantum Field Computation Model (UQFCM)

Keywords:

Quantum simulator
Quantum field theory (QFT)
Transition probability
Success probability
Qubit
Quantum field computation model (QFCM)
Universal QFCM
Quantum Fourier transform (QFT)
Quantum artificial intelligence (QAI)

ABSTRACT

Quantum field theory (QFT) simulators simulate physical systems using quantum circuits that process quantum information (qubits) via single field (SF) and/or quantum double field (QDF) transformation. This review presents models that classify states against pairwise particle states $|ij\rangle$, given their state transition (ST) probability $P_{|ij\rangle}$. A quantum AI (QAI) program, weighs and compares the field's distance between entangled states as qubits from their scalar field of radius $R \geq |r_{ij}|$. These states distribute across $\langle R \rangle$ with expected probability $\langle P_{\text{distribute}} \rangle$ and measurement outcome $\langle \mathfrak{M}(P_{\text{distribute}}) \rangle = P_{|ij\rangle}$. A quantum-classical hybrid model of processors via QAI, classifies and predicts states by decoding qubits into classical bits. For example, a QDF as a quantum field computation model (QFCM) in IBM-QE, performs the doubling of $P_{|ij\rangle}$ for a strong state prediction outcome. QFCMs are compared to achieve a universal QFCM (UQFCM). This model is novel in making strong event predictions by simulating systems *on any scale* using QAI. Its expected measurement fidelity is $\langle \mathfrak{M}(\mathcal{F}) \rangle \geq 7/5$ in classifying states to select 7 optimal QFCMs to predict $\langle \mathfrak{M} \rangle$'s on QFT observables. This includes QFCMs' commonality of $\langle \mathfrak{M} \rangle$ against QFCMs limitations in predicting system events. Common measurement results of QFCMs include their expected success probability $\langle P_{\text{success}} \rangle$ over STs occurring in the system. Consistent results with high \mathcal{F} 's, are averaged over STs as $\langle P_{\text{distribute}} \rangle$ yielding $\langle P_{\text{success}} \rangle \geq 2/3$ performed by an SF or QDF of certain QFCMs. A combination of QFCMs with this fidelity level predicts error rates (uncertainties) in measurements, by which a $P_{|ij\rangle} = \langle P_{\text{success}} \rangle \lesssim 1$ is weighed as a QAI output to a QFCM user. The user then decides which QFCMs perform a more efficient system simulation as a reliable solution. A UQFCM is useful in predicting system states by preserving and recovering information for intelligent decision support systems in applied, physical, legal and decision sciences, including industry 4.0 systems.

* Corresponding author.

E-mail addresses: phibal12@uvic.ca, philbabck_orbsix@msn.com (P.B. Alipour).

Specifications table

Subject area:	Computer Science
More specific subject area:	<i>Decision sciences, statistical mechanics, energy, physics and astronomy: quantum computing, communications, particles and statistical physics</i>
Name of the reviewed methodology:	<i>Universal Quantum Field Computation Model (UQFCM)</i>
Keywords	Quantum simulator; Quantum field theory (QFT); Transition probability; Success probability; Qubit; Quantum field computation model (QFCM); Universal QFCM; Quantum Fourier transform (QFT); Quantum artificial intelligence (QAI)
Resource availability:	Resources available to validate the review method are: 1- P. B. Alipour, T. A. Gulliver, Quantum field lens coding and classification algorithm to predict measurement outcomes, MethodsX, Elsevier, 10 (2023) 102136, Ref. [7]. doi: 10.1016/j.mex.2023.102136 . In this review, Ref. [7] is used to compare its findings with other method articles published on quantum simulation models that simulate QFTs in different fields of science employing cutting-edge methodologies to observe and predict any physical system event. Other supportive research articles used in this review: doi: 10.2139/ssrn.4229321 distributed in Elsevier e-Journals e.g., Comp. Theo. 6 (2023) 10; 2- P. B. Alipour, T. A. Gulliver, Dataset for Quantum Double-field Model and Application, Mendeley Data, Elsevier (2022) V2+, doi: 10.17632/gf2s8jkdf , Refs. [10] and [11].
Review question:	<ol style="list-style-type: none"> 1. On what classical and quantum scales the observable universe can be simulated and measured as a universal method using computers? 2. What are the notable quantum simulation methods or computation models used in simulating quantum field theories and their related sciences? 3. What limitations of quantum simulation models are reviewed? 4. What common parameters can be extracted to use and measure system states by comparing models' strengths and limitations? 5. Can there be a universal QFCM (UQFCM) developed to make a strong prediction of a system state through QAI simulation models? 6. Can a trained QFCM be embedded in other simulation models simulating physics and make strong predictions?

1. Method details

1.1. Introduction

1.1.1. Problem statement and solution

Simulating the complete physics of our universe on any scale has been a major challenge among scientists. The simulation problem begins when one wants to study events occurring in a thermodynamic system. The idea to simulate this system on the smallest possible scale, not smaller than the Planck length $\lambda_p \approx 10^{-35}$ m [2,7-9], was proposed by R. Feynman [1,27], as a quantum simulation model. Questions were raised and discussed around the possibility of building a universal computer capable of simulating the universe and answer fundamental questions about the physics of matter [1]. This requires measuring the forces that define matter and its constituents, existence, behavior and properties quantified within the observable universe. This measurement emphasizes on the statistical mechanics and thermodynamics describing the physics of matter as heat, work, temperature, and their relation to energy, entropy, properties of matter and radiation [1,2]. This measurement problem raises the question on, how to accurately observe and predict events in a thermodynamic system on a targeted scale, i.e., on a quantum or classical scale? On the smallest measurable quantity is the quantum scale, λ_p , which requires a quantum simulation computation model to compute and visualize the physics of events occurring between particles in the system.

Among current solutions, [54] proposes quantum computers as universal quantum simulators that require addressing their circuit design limitations affecting the Hamiltonian (system's total energy). Examples to observe this change in energy are the spin-type and Heisenberg models programmed and mapped to a quantum circuit under thermodynamic laws [51,52]. A universal simulator requires an effective local Hamiltonian obeying the algebra of Pauli matrices, then encoded into qubits (quantum information, or QI) by a quantum circuit [54]. The reason is, Hamiltonian models of physical interest can be expressed in locally interacting spins, e.g., Ising and Heisenberg models [38,40,54]. The fidelity and probability for measuring spin type Hamiltonians, range from an open system exhibiting disorder in noisy channels, to models that use photons, sampled and slave particles [7,26,52]. In [52], shuffling the photons' positions can detect multi-entangled photons with random probabilities. This requires the measurement of disorder in channels as entanglement entropy (EE). Particle entanglement can be predicted by measuring EE, and certified with high fidelity when determined [52], see Fig. 2. However, models like [7, pp. 3–8] propose using slave particles in implementing quantum registers to count sampled particles and their entanglement in the system. Here, the circuit simulates double-valued probabilities of spin, particle state occupation or their possible entanglement.

A universal simulator must preserve information under thermodynamics in an open system, compared to a closed system that eliminates external noise sources with no information loss. Hybrid quantum-classical simulators can be used to supply QI to the user, by which predict the next system state and retrieve previous particle states (events) over time. This is an evolutionary Hamiltonian of the thermodynamic system. Same studies [7,52,54] propose the simulation of a desired Hamiltonian using trapped ions and super-conducting quantum circuits. Certain method objectives must be met to validate such model solutions as follows.

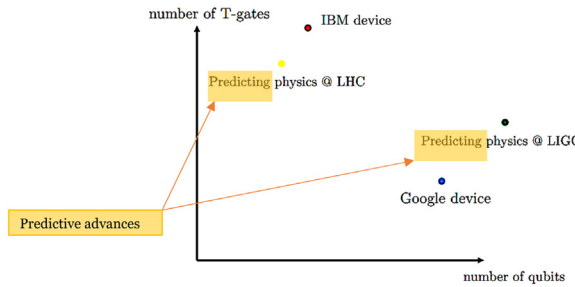


Fig. 1. An imaginary plot projected relative to predictive advances made in HEP, methods and technology. This plot includes the required computational resources needed for observations and qubit computation scale on quantum devices. The plot summarizes experimental organizations and the expected future of their technology, according to [15].

1.1.2. Method objectives and models

The current solution known to simulate and predict system events should achieve the following research goal (4th objective) and objectives (first three objectives):

1. Employ models as the 1st objective, which is a quantum field theory (QFT_h) simulation method. The method simulates QFT_h to construct physical models that measure e.g., particle interactions.
2. Compare models' limitations and strengths as the 2nd objective.
3. Visualize events, their probabilities and predict them reliably to determine system efficiency, and suggest alternative energy paths to achieve a desired Hamiltonian [7] (target state) of the system.
4. The goal is to achieve a universal QFCM (UQFCM) for the strongest system state prediction (Fig. 1) based on the results of model comparisons from the 1st through 3rd objectives.

Notable models targeting the three objectives in simulating QFT_h as discussed in this review are:

- Conformal field theory (CFT), as a strongly-coupled theory [16,40]. Examples for CFT are:
 - A quantum double field (QDF) algorithm, called a QF lens coding algorithm (QF-LCA) [7–12].
 - A universal quantum algorithm (UQA) [38] listed for simulating open systems with expected success probability $\langle P_{\text{success}} \rangle$ rates, when quantum-assisted on noisy intermediate-scale quantum (NISQ) devices [42]. From the four objectives, this qualifies as a QFCM, but not as a UQFCM.
- Quantum Fourier transformation (QFT) [7–12],
- Basis light-front quantization (BLFQ) [3–5,46],
- Discrete light-cone quantization (DLCQ) [3],
- Adiabatic quantum optimization (AQO) [40],
- Adaptive quantum optics (AQOpt) [51,52]: entangled photons resolve the time reversal of events as information is preserved under thermodynamics between subsystems as indistinguishable states.
- One-dimensional Gaussian (1DG), as a nearly optimized algorithm for generating a ground state (GS) of a free QFT_h [18] that can correspond to a classical field of free particles, Section 3.
- Lattice quantum field theory (LQFT) [5,14,16],
- Hardy's nonlocality theory (HNT) to predict entanglement by measuring EE for a particle pair interaction at a large distance [37]. This model improves the success probability in demonstrating nonlocality for n -particle HNT. Simulating this success prevents the vanishing of $\langle P_{\text{success}} \rangle \rightarrow 0$ as n grows compared to previous models of the same study [37].
- Quantum tunneling for QFT_h (QFT_h-QT) [12,17].
- QFCM for high energy physics (HEP) [13].
- QDF for any QFCM is followed by
- Quantum artificial intelligence (QAI) [7,44,45], to classify states, train and predict for a QFCM.
- Newly emerging QFCMs that achieve an improved prediction model or a UQFCM as the 4th objective, or research goal.

This solution includes addressing potential errors and uncertainties in measurements from a targeted system for any thermodynamic or statistical mechanical reason to observe in the universe. For this solution, the I/O data from QFCMs are stored as a simulation model database (SMDB). A QFCM program accesses and analyzes the stored QFCMs' measurement data for a UQFCM. See, Graphical Abstract and Table 2 examples.

Any simulation model has limitations and strengths in simulating events, and an expected measurement outcome $\langle \mathfrak{M} \rangle$. An intelligent decision (support) simulator (IDS) [7–11,57], reports these outcomes as worst-/best-case scenarios relative to an event simulated or observed from the system. A human observer via IDS, can target a desired $\langle \mathfrak{M} \rangle$. In this paper, a “desired outcome” is a specific target state (TS) defined by the observer as a desired Hamiltonian [7, pp. 3, 10 and 25–29]. This “desired Hamiltonian,” is the expected

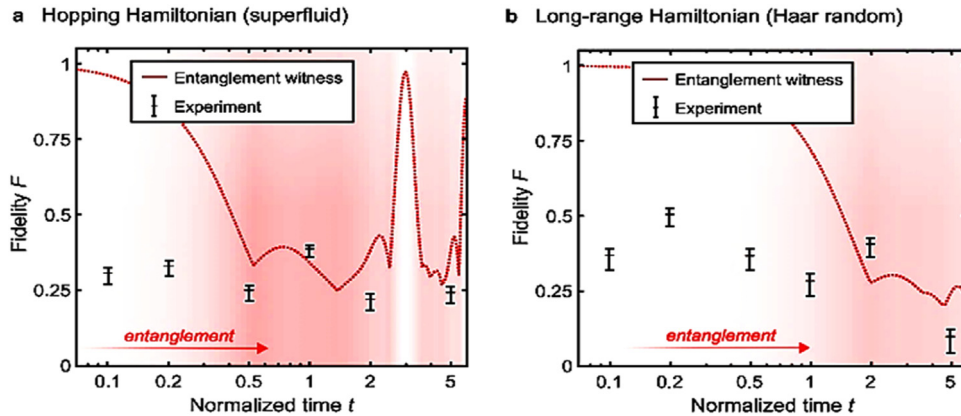


Fig. 2. An example of fidelity between the experimental and the TS (specified by the experiment to attain) with confidence values shown from the AQOpt model [52]; (a) Certifies entanglement in the hopping Hamiltonian, which consists of equal-strength nearest-neighbor interactions between all modes in simulating the superfluid, and a set of 20 randomly chosen long-range Hamiltonians; (b) Certifies entanglement in the Haar random transformation (SF transform shown in Table 1), corresponding to a Hamiltonian with random long-range interactions, and a possible built-up of longer-range entanglement. For both measurement outcomes, a higher saturation indicates a stronger presence of multi-photon entanglement [52]. Note: fidelity is scaled from min-to-max between $[0, 1]$, scaled down from $[0, \infty]$ for compatibility reasons, compared to other QFCMs. Other QFCMs' $\langle \mathfrak{M}(F) \rangle$ could be greater for a set of models as, $\langle \mathfrak{M}(F) \rangle \geq 7/5$, selecting on average 7 QFCMs that might perform this task more efficiently for a desired Hamiltonian.

total energy of the system to observe in favor of system efficiency, performance, reliability, and P_{success} . A strong prediction of particle (energy) states and their state transition (ST) in that system, produce the desired $\langle \mathfrak{M} \rangle$. This expected outcome can have a high fidelity in measurement, $F \rightarrow \infty$. The range of this fidelity can be readjusted for the expected fidelity measurement $\langle \mathfrak{M}(F) \rangle = \max F \rightarrow 1$. This is plotted in Table 1's graph and Fig. 2, for a model's measurement preference based on its $\langle \mathfrak{M}(F) \rangle$. The greater the F and P_{success} , the lesser the cost of resources to conduct an experiment and trials required to attain the expected TS.

The solution to a UQFCM is to simulate physical systems on any scale using QAI with strong prediction results over $\langle \mathfrak{M}(F) \rangle$, correlated to $\langle \mathfrak{M} \rangle = \langle P_{\text{success}} \rangle \geq 2/3$ results, performed by specific models [7–9,45]. This presents a high F in distinguishing and classifying particle states based on their distance-based classifiers [7,28–30]. Classifiers measure distance between data points and assign weights to a class to generate energy scores. An energy score is exemplified by [55], and discussed towards the end of this section.

From classifiers, QFCMs are selected to present an optimal universal measurement of QFT observables. This includes QFCMs commonality of measurement outcome, as in limitations to predict system events based on $\langle P_{\text{success}} \rangle$ over STs. The probability distribution of particle states in the system, $P_{\text{distribute}}$ yields $\langle P_{\text{success}} \rangle$, according to Eq. (3), Section 1.3. The results of measuring these probabilities are classified by a QFCM algorithm to determine F in conducting quantum measurements. Consistent results of QFCMs with high $F \rightarrow \infty$, are averaged over STs as $\langle P_{\text{success}} \rangle \geq 2/3$ performed by a QDF, or a single field (SF) transformation model. An SF transformation can obey a QFT or its inverse, QFT^{-1} , as discussed in Section 2. However, a QDF can denote both, QFT and QFT^{-1} , in its DF transformation [7–9]. One of which, is measuring entanglement between a pair of particles by QDF and QFT models, aka correlated particles [7–9,45]. Albert Einstein called this correlation, “a spooky action at a distance,” a property known as entanglement [46]. If one state is known, the entangled state can be predicted with a $\langle P_{\text{success}} \rangle = 1$, given no information loss occurs. This information is retrievable by pairwising with other particles. For example, by projecting photons between a particle pair in a communication channel [7,45,46,52], a readout can be made from the correlated (entangled) particles.

Information loss is an issue during teleportation (under decoherence versus noise) of an unknown state [9, Secs. 2.2, 4.2, 5.1], where different models, such as QDF, address the retrieving or reconstruction of information between the teleported states and their fields through a QFT, CFT or QDF transformation. This is achieved by entangling more particles with the pair, e.g., photons projecting on their entangled state within the quantum circuit. For example, these models simulate and predict phase transitions (PTs) from classical (CPT) to quantum (QPT) as Bose-Einstein condensate (BEC) in Einstein-Podolsky-Rosen (EPR) traps [7–9]. The simulation from e.g., Fig. 15, shows particle trapping from a lattice model to observe their entanglement and predict the event based on measuring EE for a desired Hamiltonian [7–11], as the 3rd method objective.

1.1.3. Review method: a QFCM case study

This paper reviews methods developed to simulate QFT and application in different fields of science using quantum circuits that process qubits via SF, QDF, QFT and QFT^{-1} . The type of field transformation is listed in Table 1 in its corresponding column. This table provides a detailed summary list on strengths and limitations for each QFCM. For example, on the limitations, a gradual improvement of fidelity by the model to predict high error rates (uncertainties) in $\langle \mathfrak{M} \rangle$ is not listed. Instead, a combination of QFCMs with QDF is proposed by weighing their $\langle \mathfrak{M} \rangle = \langle P_{\text{success}} \rangle \lesssim 1$ as a QAI suggestion to its user. The QFCM user, then decides which QFCMs perform a more efficient system simulation and measurement outcome.

Table 1

Comparison of QFCMs, their measurement data, strengths, limitations, and expected measurement outcomes relative to fidelity. Bottom shows the table's graph between the average of the $\langle P_{\text{success}} \rangle$'s and \mathcal{F} 's lower bounds, given index value n of the table, which reflects the summary of models' strengths and limitations.

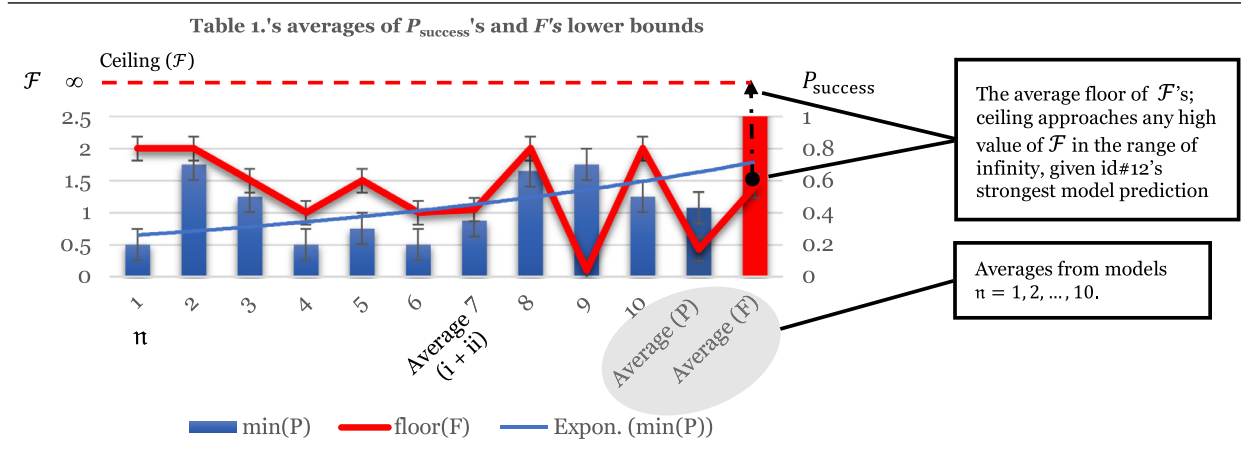
Id n	Model name; Ref. [#]	Data to measure (\Re 's); Field transform/computation type	Strength(s)	Limitation(s)	$(\Re(P))$; for quantum or classical state	Fidelity \mathcal{F} from Eq. (3)
1	CFT; [16, 38, 40]	Find a particle's state; SF transform to compute probabilities	- Consistent prediction and sampling with low error rate - Entanglement entropy (EE) and state correlation measure - Optimization in quantum state predictions	- Analog quantum simulation of the Hamiltonian not explored - QDF not possible - Limited design to simulate, needs e.g. varying number of ancilla (extra) qubits	$\langle P_{\text{success}} \rangle \geq 0.2$; ψ_i for state $ i\rangle$	$\max \mathcal{F} \rightarrow \infty$
2	iDG for QFT/GS; [18]	Find a particle in iDG state; QFT and/or SF transform [18, Sec. 3] to generate iDS and probabilities	- Entanglement entropy (EE) measure - Hybrid method in simulating particle's ground state (GS) and near GSs (Figs. 2-4) - Optimization in quantum state predictions	- QDFs or multi-field transforms for N bodies cannot be simulated	$\langle P_{\text{success}} \rangle \geq \frac{2}{3}$; ψ_i for state $ i\rangle$	$\max \mathcal{F} \rightarrow \infty$
3	QFT & QFT- [†] ; [7-12]	Find particle or its state; SF or QDF or QFT, or {QFT & QFT- [†] } on qubits	- SF, QDFs or multi-field transforms of Eqs. (2) & (3) are applied - Consistent $\langle P_{\text{success}} \rangle$ and \mathcal{F} results for EPR, BEC and trapped ions (GSs) - Information preservation of past events if QDF or {QFT & QFT- [†] } on qubits used for simulating an open quantum system	- Model's future scope not explored for all open/closed classical and quantum systems	$\langle P_{\text{success}} \rangle > \frac{1}{2}$; ψ_i for state $ i\rangle$ or ψ_{ij} for state $ ij\rangle$	$\mathcal{F} \leq \max \mathcal{F}$
4	LQFT, QFT [†] -QFT, HEP and HNT; [3-5, 12-14, 17, 19, 23, 37, 59, 60]	Error or success probability rate; SF groups to reduce errors	- Optimization in detecting/reducing quantum system errors - General predictions in potential well: quantum tunneling [12, 19, 59, 60]; high energy emissions [13] - Improve $\langle P_{\text{success}} \rangle$ against its vanishing for n particles - EE measure and detection	- Specific to stochastic or HEP systems (excl. [12, 19, 59, 60]) - Error prone at decoherence times if gate errors undetected (vanishing $\langle P_{\text{success}} \rangle$'s) - Eq. (4) applicable on N to $2N$ particle field transform causes errors if no control	$\langle P_{\text{success}} \rangle > 0.1$; ψ_i for state $ i\rangle$ or ψ_{ij} for state $ ij\rangle$	$\min \mathcal{F} > 0$
5	BLFQ; [47]	Find a particle or its state; SF transform to compute probabilities	- SF of Eq. (2) applicable	- QDFs or multi-field transforms of Eqs. (2) & (4) N/A	$\langle P_{\text{success}} \rangle \geq \frac{1}{3}$; ψ_i for state $ i\rangle$	$\mathcal{F} > \min \mathcal{F}$
6	BLFQ to DLQO; [3-5]	Find a particle or its state; SF or QDF groups to predict and reduce errors	- SF or QDF of Eq. (2) applicable - SF groups to operate on single, pairwise or multi-qubits to obtain entanglement - Fault-tolerant hybrid system	- Specific to stochastic or HEP systems - Obtain $\max \mathcal{F}$ only by min GS strategies	$\langle P_{\text{success}} \rangle > 0.1$; ψ_i for state $ i\rangle$ or ψ_{ij} for state $ ij\rangle$,	$\mathcal{F} \geq \min \mathcal{F}$
7	i. AQO; [40]	Find a particle or its entangled state; SF to predict entanglement	- Adiabatic quantum optimization - EE measure and detection - Not specific to photons to process between subsystems (industrial type QF annealing for AQO is [59]. Excluded, see	- Limited to detecting entanglement for ionic traps or particle pairs in closed systems - New model [59] is excl. for not showing high $\langle P_{\text{success}} \rangle$ with	$\langle P_{\text{success}} \rangle > \frac{1}{2}$; ψ_{ij} for state $ ij\rangle$	$\max \mathcal{F} \rightarrow \infty$

(continued on next page)

Table 1 (continued)

			limitations next, or id #4)	max \mathcal{F} values (id #4)		
		ii. AQOpt; [51, 52]	<ul style="list-style-type: none"> - QDF/QFT compatible, preserving information against any data loss due to thermodynamics [51] - Reverse Hamiltonian or event time as in id#8 citation simulated for photons to retrieve information - Fidelity certificate for certain entangled states when probability for its $\langle P_{\text{success}} \rangle$ measures from $P_{\text{distribution}}$ 	<ul style="list-style-type: none"> - Specific to photons to process - Low or random number of $\langle P_{\text{success}} \rangle$'s for all entangled states and retrieval of information 	Random $\langle P_{\text{success}} \rangle > 0$ compared to id #7.1 ; ψ_i for state $ i\rangle$ and ψ_{ij} for state $ ij\rangle$,	
8	QDF; [7-11]	Find a particle or its state; QDF or {QPT & QFT- λ } on qubits	<ul style="list-style-type: none"> - QDFs or multi-field transforms of Eqs. (2)- (4) are applied - EE measure and detection (Fig. 13) - Distance-based data classification and weights - Find alternative energy paths for particles to maximize system efficiency - Detect any quantum state under decoherence - Retrieve data or reconstruct information in case of data loss - QAI & AI for strong predictions (id #12) 	<ul style="list-style-type: none"> - Data sampling from any physical source not tested except from quantum simulators and devices (IBM-QE, QInspire, etc.) - Early physical data sampling, measures and retrievals is costly (Figs. 14-16) 	$\langle P_{\text{success}} \rangle \geq \frac{2}{3}$; ψ_i for state $ i\rangle$ and ψ_{ij} for state $ ij\rangle$, revealed as classical i or i, j for a pair of states	$\max \mathcal{F} \rightarrow \infty$
9	AI; [44]	Predict and suggest energy paths for an efficient system; distance-based data points	AI for strong classical state predictions based on classical I/O's	N/A to QFCM data	$\langle P_{\text{success}} \rangle \geq \frac{2}{3}$ if quantum state $ i\rangle$ revealed as classical i by a QFCM like QDF	$\min \mathcal{F} \rightarrow 0$ for quantum cases
10	QAI or hybrid model; all n references and [7, 43-46]	Predict and suggest energy paths for an efficient system; distance-based data points	QAI from QFCM I/O's on {IBM, QInspire, NISQ, Qkit, ...} computers for strong any state predictions	Time cost effectiveness in prediction for QFCMs	$\frac{1}{9} \sum_{n=1}^9 \langle P_{\text{success}} \rangle_n > 0.4$; for any state	$\frac{1}{9} \sum_{n=1}^9 \mathcal{F}_n \leq (\max \mathcal{F})$
11	QAI & AI Sum	Σ Data (id #) = Data ((1, 2, ..., n)); SF, QDF, QFT, (QFT & QFT- λ), other FT	Suggests efficient energy paths to user to choose n QFCMs via SMDB with strong state predictions for user to decide	If weaker models of n not deselected, sum remains for $\langle P_{\text{success}} \rangle$ values suited for > 0.4	$\frac{1}{10} \sum_{n=1}^{10} \langle P_{\text{success}} \rangle_n > 0.4$ for all n's to decide by user	$\frac{1}{10} \sum_{n=1}^{10} \mathcal{F}_n \leq (\max \mathcal{F})$
12	Universal QFCM	Data model control based on id #11 selection(s), substitution or elimination	<ul style="list-style-type: none"> - Suggests strongest prediction after model control for user to decide - Predict worst vs. best case events from QFT experiments by e.g., CERN datasets [48] imported to the SMDB 	<ul style="list-style-type: none"> - id #3 applied - id #11 applied - less interactive simulation on IDS. Solution: [46] to simulate quantum games [7, 9] 	id #11 applied id #11 applied	id #11 applied

(continued on next page)

Table 1 (continued)

The review method is *quantitative* at the early processing steps of data measure based on $\langle \mathfrak{M} \rangle$ recorded from a quantum system (event), e.g., an ST or PT describing the system's state. A QFCM estimating $\langle P_{\text{success}} \rangle$ is the target of its success probability in measurements, by which the model is classified, given its prediction accuracy. At the output stage, model validation is the review's next step. For example, validate the correctness of the claims made by the selected model from its code results on a quantum device. Depending on how consistent the model under review is in producing the expected results describing the system, the $\langle \mathfrak{M}(F) \rangle$ is evaluated relative to uncertainty measure and error rates. For instance, data loss and uncertainty increase are expected for a system's state under decoherence [7-9,37,52], e.g., an AQC program running on a D-Wave device [40]. However, the mitigation process to address data loss as a solution in reconstructing or retrieving data, can be satisfied by other models, such as QDF [7-9] and AQOpt [51,52], which discuss this $\langle \mathfrak{M} \rangle$.

The methods of control, at the high-level of models' review, are *qualitative*. This is determined after the *elimination*, *combination* of one or more models, and *substitution*. For instance, a selected QFCM is qualified for a UQFCM after reviewing the model's fidelity in estimating $\langle \mathfrak{M} \rangle = \langle P_{\text{success}} \rangle$. In fact, *will this model review from its quantitative data contribute to a high $\langle \mathfrak{M}(F) \rangle \in (0, \infty)$? Will it require QAI methods to class and rate it as being more efficient in measurements compared to other QFCMs?* The answer lies in a QAI program [7,44-46] that classifies models for its user, based on their $\langle \mathfrak{M} \rangle$'s relative to F . This model review's flow is presented by a models' control process in Table 4. The physical controls involved for observing system's I/O data, are simulated by system model components as particle controllers. For example, for an ion trap, photonic probes and sensors are used [7-9]. This includes any physical material needed to study particle thermodynamics. The study's information is used by the QAI program to simulate worst-/best-case scenarios of a particle contributing its energy to the system's Hamiltonian. The particle's quantum mechanics evaluates $\langle P_{\text{success}} \rangle$ of the particle state, by which, the next system state is predicted. This is achieved by measuring $\langle P_{\text{distribute}} \rangle$ from the sum of particle states averaged over time where $\langle P_{\text{success}} \rangle$ is yielded. These cases are simulated by QFCM algorithms written in e.g., QASM (quantum assembly language), executed on a quantum device in a lab environment where data is generated, such as IBM-QE and QInspire [33,49,50].

Quantum state measurements are handled by QFCMs, as in a QASM simulator, collapsing the state of a qubit, according to the probabilities predicted by quantum mechanics. The interpreted data are the classical information delivered to the user by a QAI program. The program suggests the user to choose a more efficient outcome (a desired Hamiltonian) in simulating and predicting a system state. This is a solution offered by the UQFCM that monitors system's output, which must satisfy all four objectives on a quantum or classical scale. In this case, data points are compared as the model's control method. This is a well-known method by QAI/AI models as a distance-based classification [30], given the weight of data point representing classical bits and qubits per measured I/O. Table 1 lists this case as id #10-12.

Simulators from [12,37,40] for specific QFT cases satisfy values of $\langle P_{\text{success}} \rangle > 1/2$. A QDF model as QF-LCA from [7-11], satisfies values of $\langle P_{\text{success}} \rangle \geq 2/3$ for any QFT. The QAI program can group and select these simulators (as an index set in Table 1) for the user to choose. This solution contributes to research method's novelty in strong prediction and measurement fidelity estimates by a UQFCM. For example, to validate $\langle \mathfrak{M} \rangle$ -data obtained on system's classical and quantum states, a quantum-classical hybrid model is proposed to run on NISQ, or on quantum-assisted devices [7-12,18,38,42-44,53], and photonic processors [52]. A quantum assisted algorithm [38] follows a UQA structure, and employs NISQ technology to reduce the quantum circuit depth and complexity when simulating open systems.

The problem with models like [38] and [53], despite their high fidelity in determining a quantum state e.g., entanglement, is requiring ancilla (extra) qubits to store partial results and obtain entanglement. For example, in [53, p. 6], circuits for different QF transformations require unitary-and-projective measurement operators. This is obtained by implementing ancillary gates that perform irreversible logical operations. This is a limitation, which requires different circuit configurations and ancilla qubits to preserve information (Table 1, id #1). To avoid this limitation, a QFCM needs to physically store information and train its algorithm for a desired Hamiltonian. For example, a QF-LCA [7] simulates a system by classifying its states, and predicts its next state with a

high $\langle P_{\text{success}} \rangle$ and F . The method is exchanging particle states within a QDF, with a fixed number of ancilla qubits. Instead, an extra qubit in [7,9] is used within the QDF when required, given the QDF's circuit configuration [7, pp. 17–23, 28]. This demonstrates model's strength in doubling the probability space for an $\langle \mathfrak{M} \rangle = \langle P_{\text{success}} \rangle \geq 2/3$. From this $\langle \mathfrak{M} \rangle$, and after state classification by a QAI program, an energy path can be rerouted to a suggested efficient path for a desired Hamiltonian. This includes EE measure to determine entangled particles, which contributes to quantifying QI against information loss in the system.

Physical data reconstruction from a damaged repository can be simulated by QFCMs based on EE measure determining entanglement. Other areas to simulate data recovery are in forensics, law, presenting accurate medical information prior to a patient's treatment, and forgery detection concerning valuables, certificates, passports, etc. In cancer research, DNA molecule reconstruction can benefit from this method. Strategies to predict virus and bacterial attacks [55], can employ quantum tomography (qubit reconstruction) [51,52], to prevent an infection spread in the human body. By having a list of selected QFCMs to combine, e.g., [7,52], the output method can then provide vital information, and reconstruct qubits in saving human lives. After an energy state classification of a targeted system, the QAI program provides its user, a set of decisions to choose as the most efficient route possible to reconstruct system states (events), for/or against, a system's $\langle \mathfrak{M} \rangle$.

The QAI [7] for [55], can provide an IDS information from simulating interactions of spike (S) protein (of COVID-19) with a number of medical herbs [55]. This information would denote the energy changes (STs) of a protein's residue relative to an interaction at different time intervals [55, Fig. 2]. The binding between the S -Protein site, and the human R -Receptor site, can determine the entanglement level between the two sites. In this method, given no information loss strategies, an atomic energy state is predicted by knowing the other entangled state from a photon readout of the two sites. The virus and the R sites' entanglement level, can determine COVID-19's growth and spread. By measuring EE, the binding reaction on the atomic level to the binding of the virus in the host can be determined. The STs, by their classical and quantum data weights and distances, are compared via QAI as energy scores. Quantum field distances between pairwise sites are measured to determine which treatment or drug is the most effective without causing side effects on COVID-19. The QDF model is a suitable example to theoretically represent this distance-based field interaction analysis [7, pp. 26–29]. As a proposal, a QDF option creates entangled states by projecting photons between unaffected R sites against the S -Protein, and predict its next state. This is by spatially creating defensive chains of entangled R sites, so to prevent the S -Protein's lock-to-penetrate cells and spreading. The predicted S -Protein state as information is shared, to program cells and defend against next targets.

The following sections present method details from the early QFCMs to current models, as a preamble to evaluate QFCMs, propose and reach a UQFCM, according to the research goal (4th objective), as outlined.

1.2. Past, present, and future simulation models

This section answers the 1st review question and objectives on what classical and quantum scales the universe can be simulated and measured as a universal method using computers.

On the *Basic Physics* lecture held at Caltech University in 1963 [1], R. Feynman addressed questions on what the constituents of the universe are in form, size, color, source, state, etc. as observables to our level of observation. Feynman's response was that, observation, reason, and experiment make up the *scientific method*. The application of this method requires finding a computer simulation of physics. According to Feynman, to make a simulation of nature, it should be quantum mechanical, as it is complex in representing the mechanics of the universe's constituents [16,27]. Intrigued by this concept, Feynman published a paper in 1982 [27] on *simulating physics and probabilities using computers*. This paper defined the probability of a diffusing particle from N -interacting particles appearing at a position x_1, x_2, \dots, x_N in state space S , at time t , [27, Section 3]. This concept satisfied solutions to the wave function $\Psi(x, t)$ in quantum mechanics which describes a particle's quantum state in a quantum system. The probability that the particle's position x will be in the interval $x_1 \leq x \leq x_N$, is the integral of the density over the interval

$$P_{x_1 \leq x \leq x_N}(t) = \int_{x_1}^{x_N} |\Psi(x, t)|^2 dx \quad (1)$$

where t is the time at which the particle was measured. For example, finding this particle at a certain point in a certain state, is the probability of success $P_{\text{success}} = 1$ or 100% probability on the prediction simulated for the particle's quantum system and position. This is also known as probability P of 1 for finding the particle in state space S .

Prior to Feynman's paper [27], comparisons within the electromagnetic (EM) spectrum in the 1920s were presented in form of a basic classification of particles, fields and waves for all matter [1]. However, in quantum mechanics, elementary particles were redefined to a many-level elementary classification of matter, with forces that move and cause their interaction on a quantum scale. This representation opposed the classical observation of massive scales defined in Newtonian physics [1]. Relation to other fields of science, such as in chemistry [16], QAI algorithms [29–31,44,45] are required to plot a detailed observation and quantification of energy and matter in the system [1]. Among which, is the study of a spin Hamiltonian in LQFTs [5,16], nuclear magnetic resonance (NMR) [26], BEC with ground states as a quantum phase transition (QPT) [7–9,25], and other related QFCMs [3,4,21]. QFCMs are compared and discussed on the overall product of their limitations, strengths in prediction, and their efficiency when it concerns system performance, Section 1.3.

Quantum field theory (QFT_h) [2], defines the concepts of particles and fields, dating back to photons as the quanta of the EM field in the 1900s by Max Planck [2]. Different interpretations were presented, such as QFT_h by Dirac in 1927 [2, Chap. 1]. QFT_h concepts were adapted to thermodynamic laws [2, Chap. 2], by using quantum computational methods to simulate thermodynamic systems and events [7-12,23]. Among which are systems in condensed matter physics, e.g., BEC [25], in HEP, e.g., the Hadron Collider (LHC) [13,15-28,48], in chemistry and nuclear physics, NMR [16]. To predict new matter forms and system states, the system's PT or ST is simulated and observed on quantum and classical scales. A preview of these models is exemplified in Section 1.1. This is not a prerequisite, but nice to have, in order to validate the selected models, their measurement results and methods. The prerequisite for this review is to focus on the key measurement parameters, $P_{\text{distribute}}$ and $\langle P_{\text{success}} \rangle$, where $\langle P_{\text{success}} \rangle$ yields from $P_{\text{distribute}}$, see Eqs. (3)-(5). These key parameters are common and visible in all these models with results, as listed in Table 1.

Examples of simulating QFT_h, are not limited to HEP or condensed matter physics in trapping particles relative to system efficiency solutions. By observing QFT_{hs}, quantum properties of particles as energy states, STs or events, can be predicted and used to reconstruct and retrieve data in case of loss. For instance, in law and forensics, reconstructing damaged documents, DNA evidence, etc., due to some accident, becomes vital to identify and classify events from the crime scene for solving a case. Detecting forged from genuine documents, requires a physical reconstruction of a damaged sample of the evidence and replicate the whole evidence by predicting what was the actual fragments of the lost information. For this, a micro-/nano-scale 3D printer [36] can be used, as discussed in Section 4. This printer operates on damaged evidence after the quantum state of the evidence's field associated to its sample has been measured. The output state from this QF association denotes the missing picture for reconstruction. The printing process is useful in reconstructing damaged or lost data, for also tracking forged banknotes, passports, and the reconstruction of damaged DNA. After DNA sampling, parts of the DNA code can be printed as strands of molecules to reprogram, see Section 4.2. In medicine, this is needed to detect cancer cells and treat patients based on DNA information, such as predicting which cells are about to get damaged. Any related field in detecting diseases, can benefit from QFT_h simulators to determine negative growth, potential cell mutations, etc., see COVID-19 in Section 1.1. Other examples are in quantum encryption-decryption algorithms based on superposition and entanglement between particles observed under a QFT, SF or QDF transformation [7-9]. Decoding qubits from a field transformation into classical bits is useful to design security systems in need of robust encryption over a communication channel. The model choice to retrieve the expected data from a noisy channel, based on e.g., QDF and AQOpt simulators [7,52], becomes vital in designing a secured channel. In industry 4.0 systems [57], an example from these simulators is to perform an efficient system based on refrigeration/combustion event, as in a heat engine. In this engine, particles that do not participate in the thermodynamic event can be predicted via QAI (Section 1.1). New energy paths are suggested over the channel for these particles to participate. The path is then rerouted to produce a desired Hamiltonian cycle (recycling an efficient heat engine), with the least negative impact to the environment. This has been explored in the proposed QDF simulation model from [7-9], which can be applied to QF annealing methods for AQO solutions [40,59].

To improve the computational performance of qubits and classical bits, hybrid models are proposed to simulate events on quantum-classical processors [18,43,44]. Efficient integration of hybrid processors and compilers are required to import or migrate resources (libraries) from classical to quantum computers, and decode qubits back to classical bits. This includes manufacturing efficient hybrid computers that simulate this process and predict efficient $\langle \mathfrak{M} \rangle$'s for a desired Hamiltonian (3rd objective, Section 1.1). For example, consider a vehicle with a self-driving option. This vehicle has a human driver who chooses an AI/QAI program to assist or make critical decisions on the road. Any latencies must be avoided in case of autonomous instant decisions are made for the driver (technology not present yet). A hybrid simulator can take QFCM predictions on the quantum scale from a QDF between the road's particle (body) field B , associated to the vehicle's field A . To anticipate motion, photons project between the vehicle's sensor field particle a , and the road's particle field b . A photon readout is made measuring the entanglement level or superposition between a and b , so to predict motion within the QDF. There are two pairwise particles interacting, and a photon superposing between a and b which has a frequency sum (time difference) or energy states $|ij\rangle$, measuring their entanglement [7-11,58]. Hence, the pair's probability space is doubled over their distance $|\mathbf{r}_{ij}|$, and state distribution. This is only possible when the particles interact on an interaction length-based scalar limit $|\kappa^2|\rho \leq 2$, from Eq. (2). From this readout and Eqs. (2)-(4), the following probability is predicted with high fidelity

$$\langle \mathfrak{M}(\mathcal{F}) \rangle_{(A,B)} = \max \mathcal{F} = P_{\text{distribute}} \xrightarrow{\text{yields}} \langle P_{\text{success}} \rangle_{(a,b)} \geq \frac{1}{3}(2) \xrightarrow{|\kappa^2|\rho(r_{ij})} \frac{1}{2}(2) = 1.$$

Compared to the hybrid model, a purely classical AI system will need enormous computational power, circuit depth and complexity to satisfy this outcome. This is unreliable for making real-time autonomous decisions on critical routes. However, the QFCM makes advanced predictions in the hybrid model based on its trainable algorithm to reach $\langle P_{\text{success}} \rangle \rightarrow 1$ per decision with $\max \mathcal{F}$, Eq. (3). This compensates any latency processing. From there, the actuation of the command to maneuver the vehicle by the classical system is executed.

In astronomy, simulating blackholes in form of a thermal BEC microscopic blackholes on a quantum scale [9, p. 3 as refs. 21-26], can achieve predictive advances in observing the universe on a macro-scale, its past, and future. A BEC experimental model [9, refs. 59-65], via a thermal BEC black hole, can provide information to predict how a pair of excited state (ES) and GS particles entangle on a scale of λ_p . A QF-LCA via QDF [7-11], proposes a QAI method based on the model's EE measure to make strong predictions of new black holes formed in the universe. This can help to hypothesize the reason for the universe's expansion [56].

Fig. 1 displays an imaginary plot projection on such *predictive models* in some areas of science and technology, including experiments conducted on QFT_{hs}, such as LHC, and laser interferometer gravitational-wave observatory (LIGO). The plot shows where in-demand devices for users require greater performance in processing massive amounts of data available on the internet and media, such as Google and IBM [12,15,22-24]. Nowadays, devices are hybridized between the quantum mechanical and classical computa-

tion models [18,43,44], as discussed earlier (or see Graphical Abstract, step 5). For example, Q-Kit is an efficient hybrid simulator for large scale quantum simulations using 20–40 qubits, with reasonable time cost (average of 26 minutes) of computation and resources. Another model is a QAI simulator using a hybrid CPU-FPGA method on current NISQ devices [44]. This information processing demands a growing integration of qubit computation using qubit gates, such as T-gates. Each gate performs a single-qubit operation around the z -axis of the qubit's Bloch sphere, aka the $\sqrt[4]{Z}$ gate [15]. For instance, fault-tolerant quantum computers will compile all quantum programs down to just the T-gate and its inverse [33].

What remains as a two-part question from [27], relevant to current quantum simulators is: What type of computer is needed to simulate physics, by which simulate physics on any scale as a universal simulator?

Note that, the simulation of “physics on any scale” denotes classical and quantum scales. However, the laws of physics break down at a distance smaller than $\lambda_p \approx 10^{-35} \text{ m}$ (λ_p is the smallest unit on the quantum scale).

The answer, relative to the advances made in the design and manufacturing of quantum computers, Fig. 1, is to study the possibility of developing a UQFCM from reliable and efficient QFCMs simulating physics e.g., [7-11,51-54]. A universal computer can then be introduced to simulate the universe. To achieve this, a UQFCM must perform with high fidelity in measurement results by distinguishing quantum and classical states. For example, a particle in a GS is distinguished from sublevels of GS, ES, and predict its next state with a great $\langle P_{\text{success}} \rangle$. An example of “predictive advances” in Fig. 1, is the data produced by LHC experiments categorized in four levels [48], classified and simulated by a QFCM. This example is illustrated by steps 1 and 7 of the Graphical Abstract via an SMDB. The four levels at CERN’s dataset portal to access and publish are [48]:

- Level 1 data provides more information on published results in publications, such as figures and tables.
- Level 2 data includes simplified data formats for outreach and analysis training, e.g., the basic four-vector event-level data.
- Level 3 data comprises reconstructed collision data and simulated data, together, with analysis-level experiment-specific software to perform full scientific analyses using the existing reconstruction.
- Level 4 data covers basic raw data (if not covered as level 3 data) with reconstruction and simulation software to produce new simulated signals, or, the re-reconstruction of collision and simulated data.

CERN’s open data portal focuses on the release of event data from levels 2 and 3, whereas LHC collaborations provide small samples of level 4 data [48]. A QFCM can import any level data to the SMDB, and simulate events based on the focused measurement of $\langle P_{\text{success}} \rangle$. The results are permissibly published from the SMDB to any CERN level. Notably, the results must satisfy the three objectives in simulating QFT_H, Section 1.1. In this case, simulate events from LHC data recorded at CERN. This is a dataset out of many QFT_H experiments conducted by laboratories publishing their data online. A UQFCM via SMDB, supplies a predictive model of events based on $\langle \mathfrak{M} \rangle = \langle P_{\text{success}} \rangle \rightarrow 1$ with max \mathcal{F} , see Eq. (3). In collaboration with CERN’s data levels, QFCM measurement results can be compared to level 3 data outputs, and give more focus on the events of CERN as predictive events. These events are compared with all four levels. This has been proposed as one of UQFCM’s strengths in Table 1, id #12. The following section discusses Table 1 results.

1.3. Review method: measurement data analysis

Measurement results are reviewed based on a QFCM’s measurement parameters used to simulate events. From Eq. (1), the probability density for a diffusing particle found in a narrow interval, in its function form is $\rho(x)$, where its units in space S are the inverse of length in d -dimensions. From the latest findings [7–9], to scale a particle’s QF during particle interactions or diffusion in the system, the product of this scalar and $\rho(x)$, can be expressed as

$$|\kappa^2| \rho(x) = P(x, x + dx) = |\Psi(x, t)|^2 dx, \quad (2)$$

where κ is an interaction length-based scalar [7–9]. Scalar κ measures the particle’s QF on any length scale, and $\rho(x)$ relates to measuring areas under the continuous-time probability distribution of particle states $P_{\text{distribute}}$ in the system. For greater variations, followed by a Δ in finding the particle, the interval range changes to greater distances of $x + \Delta x$ up to $\pm\infty$, returning a P of 1 within that range. This denotes that the particle exists and possibly found within that range.

For a pairwise particle, from [7–9], a photon field (light source) projects photons onto the particle pair’s space relative to λ_p . This can cause the pair’s interaction, diffusion, or entanglement within a QDF between their sites i and j . Each particle site has an ST probability occurring at its joint field point (a, b) , i.e., $i_{a,b}$ or $j_{a,b}$ in the QDF, which occupies S from Eq. (1) or (4). The pair’s ST probability is denoted by $P_{ij} = P_{\text{success}} \in [0, 1]$ with a density range of $|\kappa^2| \rho(x) \leq 2$, [7, p. 7]. In this case, $\rho(x)$ takes the form $\rho = \rho(k_{ij})$ or $\rho(r_{ij})$, where k is the wavevector of a projecting photon from its field measured in m^{-1} , and r is a pairwise field position vector measured in m , relative to λ_p between the pair. Scalar κ applied to a QF, transforms the field by the pair’s interaction through wave propagation and scattering between field points (a QDF projection). This field ranges between the upper and lower bounds of the scalar, $|\kappa^2| \rho \in [0, 2]$, as proven in [7–9]. The bounds of scalar k rewrite the ST probability in Eq. (3), or see [7, pp. 5–7]. The measurement outcome from k (product) operations can be observed after a Hadamard gate H in a quantum circuit. For example, a SWAP gate [41], in a QDF circuit [7], obeys the same principle as shown in Fig. 12. The exception from a QDF circuit, compared to other models, is that qubits can be recovered after SWAP due to entanglement and superposition between pairwise particles. This measurement fidelity of quantum states is specific to distance measure between states. For example, if a QFCM consistently performs $P_{\text{distribute}}$ of states computed from $\rho(x)$ in finding the particle, the greater P_{success} and \mathcal{F} by this model in distinguishing and predicting particle states in the system. The overall result of probability measurement outcomes is presented with variations observed between

QFCMs' outputs, to possibly propose a UQFCM. A QFCM's \mathcal{F} , can be determined from its $\langle \mathfrak{M}(\mathcal{F}) \rangle$ range as

$$\langle \mathfrak{M}(\mathcal{F}) \rangle_S = \lim_{\begin{array}{l} \min \mathcal{F} \rightarrow 0 \\ \max \mathcal{F} \rightarrow \infty \end{array}} \mathcal{F} = \begin{cases} \max \mathcal{F} = \left\{ \begin{array}{l} P_{\text{distribute}} \xrightarrow{\text{yields}} P_{\text{success}} \leq 1 \\ \text{for } \rho(x) < \infty, \text{ as } t > 0 \end{array} \right\} \in (\min \mathcal{F}, \infty) \\ \min \mathcal{F} = \left\{ \begin{array}{l} P_{\text{distribute}} \xrightarrow{\text{yields}} P_{\text{success}} < 1 \\ \text{for } \rho(x) < \infty, \text{ as } t > 0 \end{array} \right\} \in (0, \max \mathcal{F}), \end{cases} \quad (3)$$

where the model's minimum fidelity in measurement, $\min \mathcal{F}$, converges between nonzero values less than maximum fidelity, $\max \mathcal{F}$, and near 0 in being effective to predict measurement outcomes. This denotes some QFCMs are unreliable in predicting events, compared to those with $\max \mathcal{F}$ in measuring a particle or system state probability from state space S in Eq. (1). The condition for $\mathcal{F} = \max \mathcal{F}$, is to get the model's fidelity arbitrarily close to a finite value, as $P_{\text{distribute}}$ yields $\langle P_{\text{success}} \rangle \rightarrow 1$, to determine the next state of the system. Latest theoretical models, such as HNT [37], improved the P_{success} in Hardy's nonlocality. Its correlation to entanglement between particle pairs, was compared to their previous works with a vanishing P_{success} , as n grew to its limit. This improvement was achieved by using basis transformation and interaction on a particle pair. In comparison, a QDF transformation [7–9] is needed to double such probabilities. The proof of the QDF theory [9], represents the measurement of distance between two events or particle states. The proof, results in doubling the pair's probability space to predict their next ST occurrence. This includes the simulation of Bell's Inequality by measuring EE, and discussions around locally hidden variables to distinguish particle states and entanglement [7–9]. The QDF model [7], argues $\max \mathcal{F}$ is true for its $\langle \mathfrak{M} \rangle$'s. Both works, [7] and [37], use minimally $n \geq 3$ particles to prove their ST (or, QPT \leftrightarrow CPT) measurement results. One, [37], proves improvement in \mathcal{F} and $\langle P_{\text{success}} \rangle$ results. The other, [7], based on measurement data analysis, proves $\langle P_{\text{success}} \rangle$ doubles with $\max \mathcal{F}$ in any case. These models can be selected to input their measurement results for developing a UQFCM, relative to their strengths and limitations.

Measurement fidelity is important, and is highlighted from Section 1.1 as follows: the greater the \mathcal{F} and P_{success} , the lesser the cost of resources to conduct an experiment and trials required to attain the expected TS. A QFCM simulating with this performance, is a strong candidate to be selected for a UQFCM.

The following part answers the 2nd review question on presenting notable quantum simulation models used in simulating QFTs.

This section reviews selected QFCMs listed in Table 1. QFCMs simulating QFTs [2,18] and QFTs [7,12,23], are compared to the QDF model [7–10]. This model selection is made on the basis of model limitations e.g., uncertainties [17,26–28], error rates and strengths as P_{success} (see, Section 2), for projecting reliable predictions of the final system state, Eq. (1). For example, depending on the model's choice in Table 1, for a strong prediction outcome, devices like D-Wave can be used to run the AQO model [40]. However, current model results indicate QFCMs run their codes on IBM-QE [33], or, QInspire devices, while QX 26, 31, 34 qubit simulators run on a classical supercomputer called Lisa [49,50]. These devices are suitable for current advances made by QFCM developers using IBM-QE and QInspire platforms. This is due to ease of access, available quantum devices to run codes, open resourcefulness of Qiskit packages (libraries), online help to debug code, and timely code execution with results from trials. Of course, quantum computers can run codes suitable to their processors' configuration, e.g., Spin-4 or Stramon-5 quantum computer from QInspire [49]. A code configuration example for certain quantum processors is shown in Figs. 12 and 13, or see [7,10,11].

In Table 1, rows id #2 and #10, hybrid models are added, such as 1DG for generating a GS of a free QFT [18], CPU-FPGA method on NISQ computers [44] as a QAI model, and Q-Kit [43]. In Table 1, id #12, interactive simulators as a quantum game [46] can engage a QFCM user to simulate a decision-making quantum system or IDS [57] as e.g., a QDF game [7,9]. For example, visualize a quantum-classical game (system) participant as Alice, Bob or Eve [7,9], who exchanges information to achieve a $\langle P_{\text{success}} \rangle \geq 2/3$ in winning a prize (a TS), as a desired Hamiltonian (3rd objective). Once achieved, this is considered a strong predictive QFCM. Another strong model is AQO [40], added to row id #7.i, but for only detecting maximum entanglement through measuring its entropy for ion traps (a spin Hamiltonian, Section 1.1). This is added to compare model's strength in achieving high P_{success} 's for a closed quantum system as opposed to any other system by e.g., QDF models. As a limitation, AQO for small success probabilities requires improvements due to the increase of decoherence in an open system, as a problem observed on a D-Wave device [40]. In contrast, id #7.ii adds a random number of successful outcomes in determining entanglement applied to current models, e.g., AQOpt by [52]. In AQOpt, a photonic processor can reach $\langle P_{\text{success}} \rangle = 1$ in detecting multi-photon mode entanglement by its single-photon detectors from the output. By detecting how many photons are in a disordered channel (which built up disorder due to thermodynamic laws [51]), the photons' positions were shuffled. As a result, entanglement was maintained between subsystems. In this case, \mathcal{F} remains high for this outcome, representing full information of previous and current particle states (Fig. 2). Hence, any retrieval of particle states as past events is possible, in order to find, recreate, or reconstruct system events in a disordered quantum system. However, in Fig. 14, this time-event reversal process employs a QDF model based on high fidelity and $\langle P_{\text{success}} \rangle \geq 2/3$ selection. Compared to the shuffling of photon positions in [52], the QDF via superposition of pairwise particles, doubles the probability space of their states on the $\langle \mathfrak{M}(P_{\text{distribute}}) \rangle = P_{|ij|}$ results. This simulation outcome presents a more deterministic picture [7,8] compared to [52], in simulating random photonic events relative to EE (uncertainty) measure. One can argue for a desired Hamiltonian (3rd objective), or TS, which model is more confident in fidelity and $\langle P_{\text{success}} \rangle$ results to witness or achieve a specific experimental outcome? The answer could be an AQOpt outcome, as in Fig. 2, a QDF outcome [7], as in Figs. 13–16, or QFT/QFT⁻¹, as in Fig. 11.

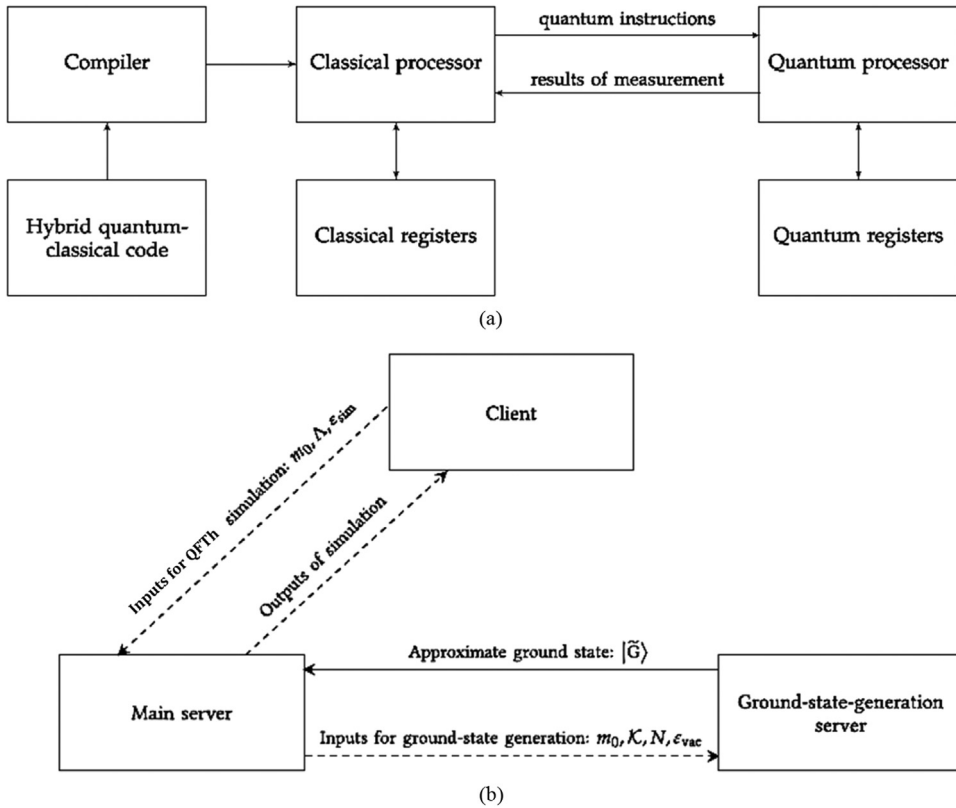


Fig. 3. (a) Hybrid model of quantum-classical hardware and code. The compiled code provides instructions to perform by processors on their associated registers. The quantum processor sends the measurement results back to the classical processor [18]. (b) A client-server framework for simulating QFTTh representing quantum communication and GS generation servers. These servers simulate massive scale bosonic QFTTh. The output from the server is an approximation for the free-field GS [18].

The significance of measurement results listed in Table 1 and their averages' graph, is to gauge the model's ability in determining system states on any scale. For example, using quantum-classical hybrid processors [11], Fig. 3, can show how the system evolves over time in a QFCM simulation. The UQFCM must at least satisfy the exponential trendline on the average minima of P_{success} 's shown in the graph, according to id #12's data model control. Table 4 illustrates this model control mechanism. Generally, each quantum simulator employing one or more QFCMs, should in its code check and see if it meets the expected measurement outcome and fidelity for a simulated event. An event can be observed as superposition, entanglement, interaction, etc., between particles in their GS, ES, or energy sublevels. By determining this ST, as an event occurring between their states, the next system state can be predicted. Specifically, to see if the \mathfrak{M} 's hit and match the $\langle P_{\text{success}} \rangle \lesssim 1$ of the $\langle \mathfrak{M}(P_{\text{distribute}}) \rangle$ on that event, e.g., presents an ST of GS \rightarrow ES among other interacting particles as the next system state. Hence, this model is reliable to apply, as it can contribute to a decision suggested by an IDS to the user [7–11]. This suggestion can be in any form of predicting events reliably, as a strong prediction outcome based on $\langle P_{\text{success}} \rangle$ results, which determines the model's $\langle \mathfrak{M}(\mathcal{F}) \rangle$.

The collected data from QFCMs (their \mathfrak{M} 's) are described under “data to measure” column of Table 1. This column, highlights where the QFCM suggests efficient ways for simulating events. For example, id #8 shows a QDF method to reroute energy paths as the updated data to analyze. As a result, more accurate models are developed to assist users to decide on the most efficient energy path to improve system efficiency. This can be validated by Table 1's graph, showing an average measurement fidelity of $\langle \mathfrak{M}(\mathcal{F}) \rangle \geq 7/5$ points. This result can be interpreted as 7 optimal QFCMs (graph bars) over 5 less (or the least) optimal QFCMs, $\langle \mathfrak{M}(\mathcal{F}) \rangle \geq 1.4$, in classifying states. From the result, the IDS selects efficient QFCMs to predict $\langle \mathfrak{M} \rangle$'s for the UQFCM user.

This review proposes the possibility to develop a UQFCM in a decision flow model diagram (see, Graphical Abstract), based on model comparisons to address each question raised in the review's specifications table. Conclusions are drawn from the review's observations from literature, summary measurements and analysis. In summary, a UQFCM gives a more focused method of measuring physical systems by presenting a unified solution to their prediction problems. The study and development of technologies from the physical world on an industrial scale can be cost effective when a UQFCM is achieved, as it improves system design, state control and performance of those technologies.

Section 2 presents QFCM limitations and model examples on how to address them. Section 3, compares a select set of QFCMs, discussing their strengths, limitations, expected measurement outcomes and fidelity from Table 1. This section lists the summary of its findings in Table 4, which contains a model control process that achieves a UQFCM. Finally, Section 4 explores some practical

examples that can hypothetically employ QFCMs, for a UQFCM, from [Table 4](#). This section also presents a new algorithm to simulate measurements of a discussed example for a UQFCM, and model's future scope based on its findings.

2. Method limitations

This section answers the 3rd review question on quantum simulation model limitations

The current method limitations in the development of a UQFCM are:

- A low expected ST probability, or a weak prediction of a measurement outcome, is noticed in a QFT system. This measure of ST probability as $\langle P_{\text{success}} \rangle$ relates to the prediction of the final system state relative to a given input (see [Table 1](#), columns \mathfrak{M} and $\langle \mathfrak{M}(P) \rangle$).
- The scattering of states is partially observed in the Hamiltonian among interacting particles, relative to their (preparation of) initial states [28]. This is significant in observing the evolution of a thermodynamic system from its initial state, to current, and final state(s), in a predictive QFCM. This is by determining the value of P_{success} described in [Table 1](#), as the ability to simulate the Hamiltonian.
- The fidelity of measuring the GS and ES, can be very low as the system evolves, due to system noise and uncertainty. Relative to system model steps, $P_{\text{distribute}}$ is measured compared to $\langle P_{\text{success}} \rangle$ in predicting the final system state, according to [Eq. \(3\)](#).
- The selected QFCM cannot adapt to other models. Is there a way to improve measurement limitations and prediction level by combining the model with other QFCMs, for a high $\langle P_{\text{success}} \rangle$ and $\langle \mathfrak{M}(F) \rangle$?

Feynman in [27], was concerned about simulation limitations on an isolated part of nature with N variables that could require a general function of N variables. If a computer simulates by computing this function, then doubling the size of nature ($N \rightarrow 2N$) would require an exponential growth in the size of the simulating computer. Thus, a QFCM needs to compute the P of configurations relative to this computational limit. The exponential growth of ($N \rightarrow 2N$) results in P of events approaching $2^{-N} \rightarrow 0$ [26–28]. This $P \rightarrow 0$ result is avoided by satisfying its complement $P' = \langle P_{\text{success}} \rangle \rightarrow 1$ using current QFCMs that reconfigure and process qubits (QI) and classical bits in a hybrid model, see e.g., [Fig. 3](#). This processing is part of an I/O data control mechanism in [Table 4](#). Higher layers of prediction are developed based on the recorded ST probability data and its distribution focused using QF lenses, and distance-based classifiers [7–10,29–31], Section 1.1. From [Eq. \(2\)](#), a QAI program weighs and compares the focused field (lens) distance d between pairwise states as qubits observed from their scalar field of radius

$$R \geq |\mathbf{r}_{ij}| : \langle \Psi^2 d^2 \rangle = |\psi_{ij} \mathbf{r}_{ij}|^2.$$

These $|ij\rangle$ states distribute across $\langle R \rangle$ with a $P_{\text{distribute}}$, and $\langle \mathfrak{M}(P_{\text{distribute}}) \rangle = P_{|ij\rangle}$ for their expected output, decoded into classical bits, or see [Table 2](#). Furthermore, a QDF coding model proposed by [7–10], addresses Feynman's exponential growth problem about N , by transforming a quantum SF to a QDF via κ from [Eq. \(2\)](#). This is achieved by measuring the fields' superposition and entanglement, aka EE, [7]. Here, the uncertainty is reduced in measuring $N \rightarrow 2N$ across $\langle R \rangle / |\mathbf{r}_{ij}|$, to the point of $\langle P_{\text{success}} \rangle$ of the system state as

$$\langle P_{\text{success}} \rangle \xrightarrow{\langle R \rangle / |\mathbf{r}_{ij}|^{-1}} \langle P_{NS} \rangle = \int_0^1 \int_0^N N_S(a, b) N \, da \, db = \left\{ \frac{1}{3}, \frac{2}{3}, 1 \right\}, \quad N_S(a, b) \in \{1, 2, 3\}. \quad (4)$$

This equation is a quantum operation against the exponential growth $2^{-N} \rightarrow 0$, or, with a $\langle P_{\text{success}} \rangle \geq 2/3$ as a *discrete solution* between pairwise field points $(a, b) \in S$ in their joint pdf $N_S(a, b) \geq 2$. These points are correlated, depending on a particle pair interaction exchanging QI between these points [7–10]. Their joint pdf for a QDF is $N_S(a, b) = 2$, and a 3rd field carrying the QI about the particle pair, returns an average value of N in [Eq. \(4\)](#) integral. For an SF transformation obeying a QFT, prior to a QDF, is $N_S(a, b) = 1$ with a $\langle P_{\text{success}} \rangle = 1/3$. There is no 4th or N^{th} field point for the joint pdf beyond (a, b) . The reason is, for a set of pairwise interactions of $N \geq 2$, a possible entanglement or superposition between these points (particles) denotes one particle pairing up to $\mu_{a,b} = (N^2 - N)/2$ particle pairs interacting in the simulation model [7]. This conforms to the P_{success} relative to error rates observed and corrected on N to $\mu_{a,b}$ qubits. Examples are reported in QF annealing readout models [59,60], and $\mu_{a,b}$ degrees of freedom in programmable spin Hamiltonian architectures [40, Section 2]. Entanglement entropy between pairwise spins of two subsystems, is measured as a function of their coupling over interaction length L . This measure determines the probability of particles entangled between the subsystems. Length L via κ from [Eq. \(2\)](#), depending on the degree of entanglement, can scale to entanglement length L_e which provides QI on the system state [7, pp. 5–7]. From [7–11,39,40], EE is determined between pairwise particles for two possible cases, “Cases 1 and 2,” as listed in [Table 2](#). These lists are extracted from [7, Table 4], given the number of sampled particles between two subsystems of a heat engine (thermodynamic system), see Section 4.1. The bottom plot of [Fig. 13](#) shows the expected measurement outcome $\langle \mathfrak{M}(P, \psi_{ij}) \rangle$ for all cases of particle sampling and interactions in the system. In the plot, the $P_{\text{distribute}}$ of particle states yield $\langle P_{\text{success}} \rangle$, according to [Eq. \(3\)](#), for all cases in [Table 2](#).

In [Table 2](#), the expected measurement result, $\langle \mathfrak{M}(P, \psi_{ij}) \rangle = \langle P_{\text{success}} \rangle \rightarrow 1$ is consistent with $\langle \mathfrak{M}(F) \rangle_S = \max F$ from [Eq. \(3\)](#) in measuring states under a κ -based QDF transformation by [Eq. \(2\)](#). This transformation doubles the state probability output relative

Table 2

Measurement data on an SMDB from a QF-LCA [7]. The SMDB lists predicted probabilities from the input of an SF to a DF (or QDF) transformation of a group of qubit pairs for an $\langle \mathfrak{M}(P, \psi_{ij}) \rangle$ of their energy state. The states are 0 for a GS, 1 for an ES, 2 for a quantum state, such as superposition as 0 and 1 (within m sideband levels of GS [7, Example 4.B]), and 3 for a complement pair condition. For example, in binary $\underline{b}(ij)$ for a P_{ij} as in the rightmost column, denotes superposition, entanglement, or a classical state for a particle (qubit) pair. If $P_{ij} \geq 2/3$ for $\underline{b}(01) = 1$ or $\underline{b}(10 \leftrightarrow 0_m 0_n) = \{0, 2\}$, then its complement on both outcomes $P'_{ij} \leq 1/3$ is $\underline{b}(11) = 3$, according to Fig. 13's lower graph results. Consult Fig. 13(b)'s EE scaling graph for the two cases. The associated probabilities to each energy state, as classified and predicted in an experiment, is weighted according to energy state profiling via QAI [7,31]. The classification for a combination of pairwise spins between particles is determined by particle pair's level of entanglement measured by L (interaction length) scaling the Hamiltonian (e.g., Ising model [7-11,40,60]) as EE scaling [7]. This is determined by measuring the expected magnetization $\langle M \rangle$, which classifies pairwise particle spins in e.g., QDF lattice traps ranging from the least, $M = 0$, to the highest level of magnetism between particles (Fig. 15(a)). This includes the expected outputs measured from the dynamics of the QDF circuit as distance-based data points [7, pp. 25-29], according to the code used for a QDF circuit in Figs. 12 and 14.

n	Case 1: $\langle \Delta N \rangle = \mu_{ij}$ for $ \langle \mu_d \rangle $	Case 2: $\langle \Delta N \rangle < \mu_{ij}$ for $ \langle \mu_d \rangle $	$f_{ \Delta_{21} }$	$\langle \Delta \Omega_{AB}^\pm \rangle$	$\langle M \rangle$	$\langle \mathfrak{M}(P, \psi_{ij}) \rangle = \left\{ P_{ij} \geq \sqrt{\frac{2}{3}}^2, P'_{ij} \right\} \underline{b}(ij) \rangle$
1	$1/\sqrt{2}$	$[\{1/\sqrt{2}, \sqrt{2}\}, n+1=2]$	$[\{0,1/\sqrt{2}\}, 1.3]$	$< \frac{1}{3} L_\varepsilon^{-D}$	0	$\underline{b}(1) = 1$
2	1	[1.5, 3]	[.5, 2]	$\leq L_\varepsilon^{-D}$	≥ 0	$\underline{b}(00,10) = \{0, 2\}$
3	1.22	[1.63, 4]	[.4, 2.78]	$\leq L_\varepsilon^{-D}$	≥ 0	$\underline{b}((00,00+10),1) = \{\{0, 2\}, 1\}$
4	$\sqrt{2}$	[1.767, 5]	[.35, 3.5]	$> \frac{1}{2} L_\varepsilon^{-D}$	> 0	$\underline{b}(((0, \mathcal{E}(\{10,00\} \xrightarrow{\text{swap if } 10} \{01,00\})),1),1) = \mathcal{D}(\{(01,10),01\}, t^*) = \{P_{01}, \underline{b}(01), P_{11} (\underline{b}(10) + \underline{b}(01))\} = \{1, 3\}$
5	1.58	[1.897, 6]	[.31, 4.42]	$> \frac{1}{2} L_\varepsilon^{-D}$	> 0	$\underline{b}(((0, \mathcal{E}(\{10,00,0\} \xrightarrow{\text{swap if } 10} \{01,00,0\})),1),1) = \mathcal{D}(\{((01,00),10),1\}, t^*) = \{P_{01}, \underline{b}(01), P_{11} (\underline{b}(10) + \underline{b}(1))\} = \{1, \{2, 3\}\}$
6	$\sqrt{3}$	[2.02, 7]	[.28, 5.27]			
7	1.87	[2.1, 8]	[26, 6.13]			
8	2	[2.25, 9]	[.25, 7]			
9	2.12	[2.357, 10]	[.237, 7.88]			
10	$\sqrt{5}$	[2.46, 11]	[.224, 8.76]			
\vdots	\vdots	\vdots	\vdots			\vdots
N	$\sqrt{N/2}$	$< \infty$	≥ 0	L_ε^{-D}	≥ 0	$\langle \mathfrak{M}(P, \psi_{ij}) \rangle = \{1, \{2, 3\}\}$

to input in particle position and energy from the QDF circuit. Notably, the *reversible time* and information preservation are true for both, the QDF and AQOpt, in retrieving previous system states (events) relative to variational thermodynamics of the Hamiltonian [7-9,51,52]. These models are in agreement between the deterministic and random results (semi-/non-deterministic [9]), id #7, compared to id #8 in Table 1. However, a QDF model (QF-LCA) achieves the doubling of P 's in its spatial transform, giving a more deterministic picture of STs compared to AQOpt [51,52]. An AQOpt, simulates events based on randomness with P 's yielding from $\langle P_{\text{distribute}} \rangle$, to locate photon pairs and their entanglement. This model measures with high fidelity in certifying entanglement

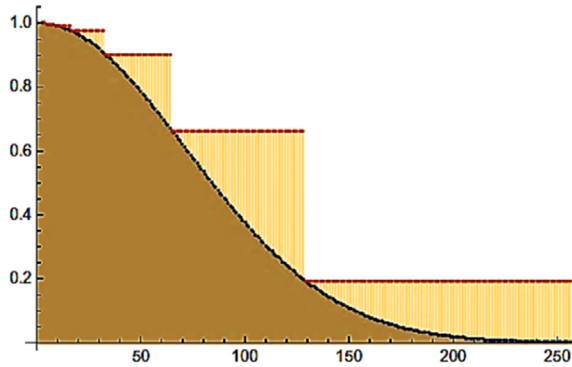


Fig. 4. A state generation step illustration. A state is prepared with amplitudes according to the orange points (step lines). Then, an inequality against the blue points (the curve) is tested. The success probability is $\geq 70\%$.

after a number of trials, hitting the right $P_{\text{success}} \approx 1$ from $P_{\text{distribute}}$, as its TS. However, SF and QDF can be applied to AQOpt under randomness if unitary gates transform where photons entangle [52], Section 1.2. One subsystem against another subsystem benefits from randomness due to photons shuffling positions (superpositions) between subsystems, as if all were entangled. Thus, the missing information in one subsystem disappears to the other subsystem [51], and so the information is preserved. In comparison, QF-LCA returns $\langle P_{\text{success}} \rangle = 1/3$ with max F denoting subsystems' information is preserved. Even in case of data loss due to decoherence, the superposition between particle pairs preserves their information within the QDF [9, Section 2].

The following section discusses a select set of QFCMs' strengths and limitations, and compares them in measurement and performance in simulating systems relative to their classical and quantum limits. The random version of models, given their limitations, such as [50,51], are not presented, but will be part of QFCMs' future scope to include when $\langle \mathfrak{M} \rangle$'s are aligned to consistent $\langle P_{\text{success}} \rangle$'s and not just $\langle \mathfrak{M}(F) \rangle$.

3. Model comparisons

This section answers the 4th review question on listing common parameters that can be extracted to use and measure system states by comparing models' strengths and limitations.

To achieve a UQFCM, comparisons should be made between the selected QFCMs employed in Section 1.2, classifying model strengths and their limitations to simulate QFTs. The limitations raised in Section 2 are noticeable relative to efficiency and expectations on ST probability and prediction factors of each method employed by a QFCM [5-12,18]. Limitations over system efficiency and state predictions, can be determined by QFCMs that simulate a quantum system from QFT and spin transformation operators. These operators describe an experimental event expected to occur from the simulated system. For example, in [18], complex methods were introduced and used to mimic classical and QFTs by their algorithms. The complexity for processing basic functions were analyzed. Examples are eigenvalues associated with the state (vector) GS, i.e., near GS $|\tilde{G}\rangle$ shown in Fig. 3, and ES of the Hamiltonian in executing a quantum circuit. From there, the program sends QI to a classical processor as a hybrid code to analyze quantum measurement results comprehensive to a human. Their research, [18], involved the generation of different bounds of GSs through hybrid algorithms. This is needed to classify and determine particle states from a classically generated GS (from a free-field GS state), as a multidimensional Gaussian state in Fig. 4. This was measured relative to particle mass, as opposed to waves, i.e., wavelet simulation through a wavelet algorithm [18].

In comparison, from [7-9,12], a universal approach is proposed to simulate QFT and QDF measurements. This was by focusing ST probabilities and their distribution based on kinetic and potential operators. A QDF algorithm, QF-LCA, makes consistently strong predictions via $N_S(a,b)$ acting on N in Eq. (4) from a continuous solution. This is only in case of some or all of the QI are exchanged at field points a and b , as

$$\langle P_{\text{success}} \rangle \cong \frac{1}{3} \times N_S(a,b) \in [1, 3] \rightarrow \left\{ \frac{2}{3} \rightarrow \dots \rightarrow 1 \right\}, \quad (5)$$

which denotes a quantum particle space in probability doubles and grows in P_{success} for determining the next system state. This is a DF computation method that decodes from its QDF circuit, a classical state, for making strong predictions based on the QDF's kinetic and potential operators [7-12]. These QFCMs are compared at the end of this section, and their I/O data control with other QFCMs in Table 4, to choose from for a UQFCM.

In Fig. 4, $P_{\text{success}} \geq 0.7$ reflects the success probability of observing future system states, given the analyzed data in the QFCM's simulation comparisons for [18], from Table 1. As discussed above, [18] simulated the quantum physics for a massive scalar bosonic QFT. This work introduces a client-server framework for simulating a QFT on a quantum computer. The model discusses the metric in use to measure the algorithm's time complexity, as well as its runtime and error rates. Different examples of QFCMs benefiting from this model and other hybrid types, e.g., QF-LCA [7], with results, are given in Secs. 1.2, 1.3, 2, Tables 1 and 4.

Table 3

Simulating QFTs using different QI methods as discussed in [16]. The lattice and conformal truncation methods are compared. The tools for using existing QI tools simulate QFTs describing the physics of lattice and quantum N -body models. Without the lattice, the authors could use methods in quantum chemistry to simulate conformal truncation.

Treatment	Starting point	Existing toolbox in QI
Lattice regularization	Usually-free theory	Quantum many-body physics
Conformal truncation	Strongly-coupled theory (CFT)	Quantum chemistry

In [16], the algorithms work for general Hamiltonians with sparsity. The model makes direct analysis of the conformal truncation of the Hamiltonian by measurement. The quantum chemistry method to describe this Hamiltonian was implemented based on the CFT, as shown in Table 3. This review finds CFT to suggest from a distinct light-matter interaction regime, the interaction is manifested in coherent oscillations of energy between matter and a photonic subsystem. CFT is a starting point to implement the QI building block as a simulation tool in quantum chemistry. Examples of this tool can be explored to simulate QF formations between particles that entangle at different magnetic moments, which exhibit different energy states. Lattice models are some examples that require the measurement and programming of spin Hamiltonians [40,60]. Another example is the strongly interacting Rydberg atoms which are in a high energy state (of the hydrogen atomic model). A Rydberg state can be used to combine BEC and Rydberg atoms at near absolute zero temperatures and simulate a new state of matter, e.g., an exotic state called a Rydberg polaron. A recent study [56], discussed limitations on how to incorporate gravity into QFT, where excited Rydberg atoms enabled the measurement of gravitating properties of the vacuum. This can give information to simulate and predict the vacuum energy and the expansion of the universe in QFT. All these examples can be classified and predicted by a UQFCM through a QAI program, model control, and selection process (see Table 4 or Section 1.3).

To validate the method proposed in [16], the study firstly performs some numerical experiments in IBM-QE [33]. The study secondly discusses quantum simulation with/without noise and treatment about noise mitigation in most measurements. The experiments are performed by a quantum simulator backend called `qasm_simulator` (an IBM QASM simulator) [33], on a quantum device `ibmq_armonk`. The quantum programming language was QASM in Qiskit as an open-source SDK platform working with quantum computers. The encoding was made into a three-qubit matrix. This review concludes that the study opened a novel approach to solve QFT simulation algorithms on quantum devices.

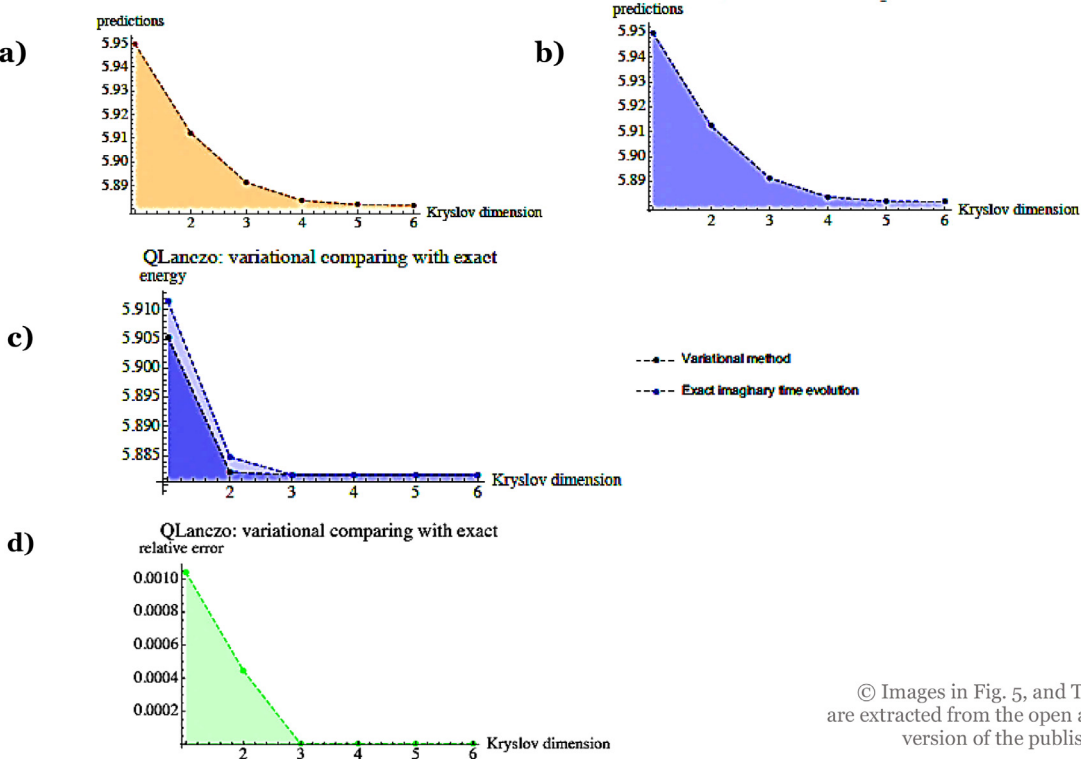
With the aid of quantum devices, the measurement results can contribute to the development of a UQFCM. The method is an explicit form of Hamiltonian for a given conformal truncation problem imported in a quantum setting. An analog of `Qiskit.chemistry` is an existing package in the IBM-QE environment. Examples of this package are functions and operators imported for experimentation with chemistry domain problems, such as determining GS and ES energies of molecules. An operator from a `core.Hamiltonian` class can be used to map e.g., a `FermionicOperator` to a qubit operator. The molecule's energy state is computed at its dipole moments, such as its nuclear repulsion energy. The molecule data results can be used to classify GS and ES energies, such as using classifiers by other QFCMs via QAI, see Section 1.1, or [7].

This review finds [16] presented ideas for preparing states and observe the Hamiltonian's real-time evolution in experiments. This included ideas about analog quantum simulations. For example, Fig. 5 shows the algorithm's prediction level compared to the actual expected results between the classical and quantum Krylov dimensions. Krylov subspaces are used in algorithms to find approximate solutions to high-dimensional state space, and observe the Hamiltonian's time evolution. This observation was simulated in [16]. The study discussed digital and variational simulations, yet, analog simulation was not explored, Table 1, id #1. This is required for a UQFCM to mimic all possible event scenarios expected in a thermodynamic system being measured on its classical and quantum energy spectra i.e., the statistical mechanical limit of N particles [32]. However, this paper discussed how the analog representation of their code could be achieved.

In the analog simulation, the paper proposes encoding quantum states into some physical models made by, for instance, Rydberg atoms. A general universal application to this model is limited to a specific range of particles in a specific environment. Some defined examples are, 2D conformal Hamiltonian models of N particles with local interactions in a lattice (between lattice sites) [16], or see lattice sites in a QDF [7–10]). Through the paper's error mitigation program, as an optimizer, a 0.26% error rate was reduced after 20,000 measurements conducted on a noisy quantum circuit by an IBM quantum computer [16].

In [5], the effect of gate errors from an LQFT-based model was shown and discussed to perform the optimal use of energy for a quantum state. This was determined by simulating quantum gates in IBM QASM simulator (Qiskit). For example, minimum-energy and maximum-fidelity strategies are used to approximate the odd and even parity GSs (Fig. 6). The optimization level is determined by studying the rotation angle of quantum gates. This includes where and when the maximizing of angles is needed to achieve optimization as the optimal choice or strategy. In this model, a hybrid quantum-classical LQFT workflow is proposed. The flow shows that interpolating operator constructions are optimized in auxiliary small-scale quantum calculations. These calculations are used to study isolated bound states, and increase the precision at fixed statistics. This accelerates principal large-scale LQFT calculations on classical computers. The principal classical calculations are robust to noise that enters quantum computer calculations. The systematic uncertainties that arise from matching between the two calculations were measured at different physical volumes, e.g., lattice spacings and truncations on the gauge field space from the quantum calculation.

An example of minimum-energy strategy is preparing three qubits in a GS, Fig. 6(a). This is denoted as $|q_1 q_2 q_3\rangle = |000\rangle$ by acting on a variational ansatz quantum gate $U(\beta^{\pi+})$. This operation consists of a sequence of single qubit rotation gates and entangling two-qubit



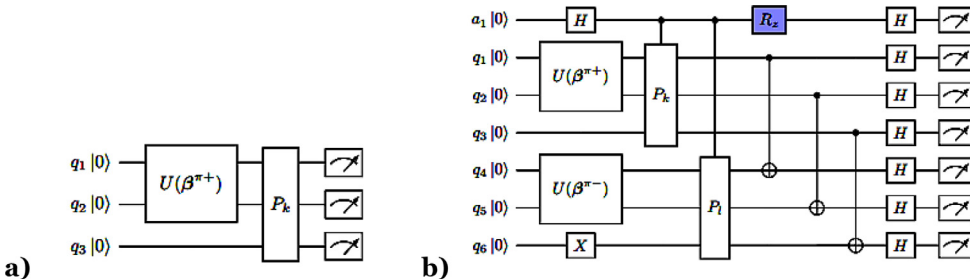
© Images in Fig. 5, and Table 3 contents are extracted from the open access, preprint version of the published paper, [16]

Fig. 5. (a, b) Classical and quantum simulations using different Krylov space dimensions, taking maximum scaling of dimension (matrix truncation) of 16. In the quantum simulation, the space span of the dimensions was diagonalized; (c) the algorithm's variational version behaved better than the exact version of this sample; (d) the relative error rate is very small, indicating that in these trials, the quantum implementation can achieve an efficient method of measurement sampling and prediction.

gates, here on $|q_1 q_2\rangle$. This is followed by applying $|P_k\rangle$ as a 3-qubit Pauli string on $|q_1 q_2\rangle$. When followed by measurement gates, the minimum-energy strategy is obtained. For implementing a maximum fidelity strategy, the circuit in Fig. 6(b) estimates the overlap of quantum energy states. This is expected to occur in a QPT or a quantum vacuum state (lowest possible energy, or, zero-point field [2, p. 8]), by implementing different quantum gates, such as a Hadamard gate [H]. A Hadamard gate can be used to convert a qubit from a clustering state to a uniform superposed state.

The results of the measurements of energies, with and without noise, based on the minimum energy and maximum fidelity strategies, are presented in Fig. 7. These results correlate to the claims made in this study as an effective and efficient way of measuring quantum energy states during STs.

The research by [37] used IBM-QE devices to simulate nonlocality in Hardy's context. Its method improves success probability $\langle P_{\text{success}} \rangle > 0.1$ in demonstrating nonlocality for an n -particle HNT, compared to their previous studies where $\langle P_{\text{success}} \rangle \rightarrow 0$, as n grew. Their measurement results are affected due to gate errors at decoherence times in the simulation, if not optimized. In their findings, EE is measured to determine the correlation between nonlocality and entanglement. An optimization solution to [37] via [3–5] methods



© Images in Figs. 6 and 7 are extracted from the open access preprint, [5]

Fig. 6. (a) Minimum-energy strategy quantum circuit implemented; (b) quantum circuit to implement maximum fidelity. This circuit uses quantum gates for a Hadamard-overlap test to achieve maximum fidelity. In this circuit, quantum states from a GS state are prepared for a probable QPT using SWAP, [H], and measurement gates. SWAP is performed using CNOT, [H], and measurement gates. The colored rotation gate on an ancillary qubit denotes the rotation about the z-axis by an angle $-\pi/2$.

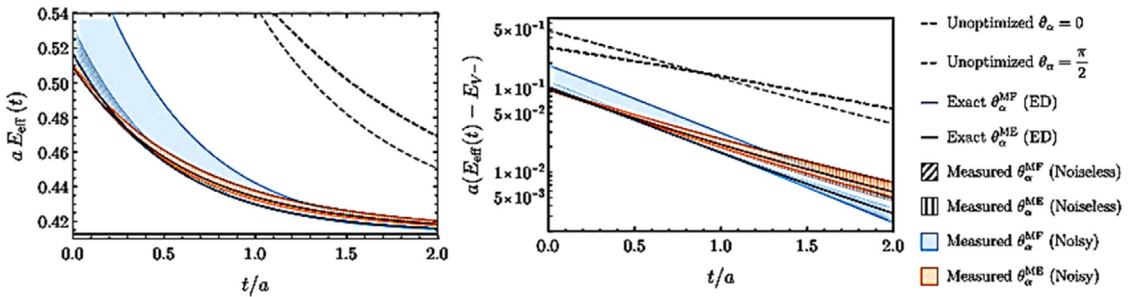


Fig. 7. Effective energy functions compared as energies are converted into lattice units of a rescaled Hamiltonian. These functions are computed from correlation functions with optimized and unoptimized interpolating operators, with and without the effects of noise in the quantum device. Solid bands (labels) encompass 100 curves from multi-shot measurements in the quantum simulation with and without noise. Left image shows the effective energy functions and their asymptote, while the right image shows the excited state values (ES contamination to allow a GS dominance at earlier t 's) in each function, on a logarithmic scale.

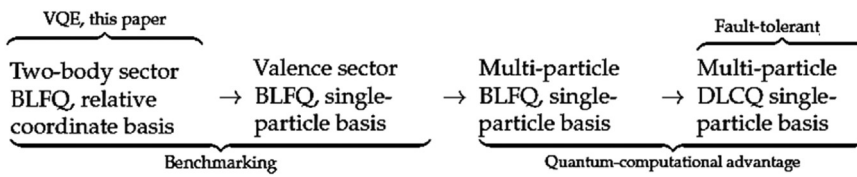


Fig. 8. Quantum simulation of the light-front QFT at different stages of complexity including resource requirements. Discrete light-cone quantization (DLCQ) is considered to be a special case of BLFQ that employs a plane-wave basis, and may be useful in the fault-tolerant quantum computing regime [3]. The rightmost (DLCQ) stage is separated due to classical preprocessing used in BLFQ to obtain approximations using fewer quantum resources.

can be applied. For example, IBM-QE devices are recalibrated for specific rotation gates and transformations. This addresses gate errors to achieve accurate quantum prediction results. In comparison, a QDF model [7] can be employed to improve success probabilities in the HNT context. For example, while Table 1 lists the strengths and limitations for HNT and QDF, a QAI program can address HNT limitations through the I/O model control process for a UQFCM. One QAI method would be classifying the $\langle P_{\text{success}} \rangle$'s of QDF and HNT. Then, a hybrid of QDF and HNT $\langle M(P) \rangle$'s at decoding makes a strong prediction in the HNT (see Table 4, Secs. 1.2 and 1.3).

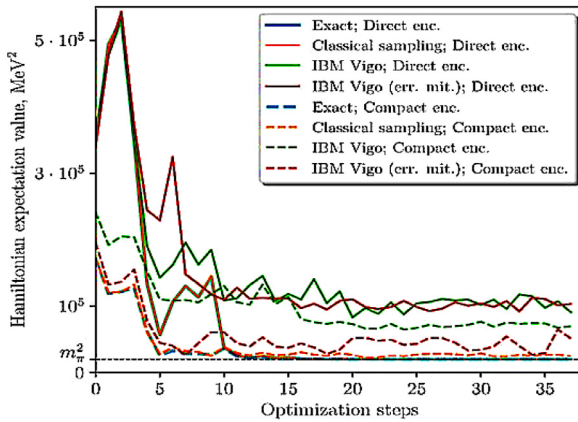
In [3,4], a quantum algorithm was presented for QFT_h simulation in the light-front formulation. The study demonstrated how existing quantum devices can be used to study the structure of bound states in relativistic nuclear physics. For example, in [3], an efficient Hamiltonian formulation of QFT_h was proposed by using the framework of basis light-front quantization (BLFQ) for solving QFT_h problems. This required the calculation of hadronic spectra, mesons and their light-front properties. Fig. 8 shows a fault-tolerant quantum computing model that simulates QFT_h involving observations of energy emissions coming from particles in LHC experiments.

In Fig. 9, and its corresponding table results, such as fractional errors expressed as percentages in estimates of various observables were calculated in the GS. The observables are pion mass squared m_π^2 , mass radius squared $\langle r_m \rangle^2$ and decay constant f_π . These were obtained from 8192 samples per term on the IBM Vigo chip, with and without measurement error mitigation. Classical sampling from the exact $P_{\text{distribute}}$ achieved values (0, 0.9] for direct encoding, and less than 44% for compact encoding. The observables are constant as physical units, otherwise are measured values. The constant terms are different between direct and compact encodings. Hence, direct and compact entries in the “no constant” rows, correspond to different physical observables, and not to be compared. For example, for m_π^2 , the exact m_ρ^2 is used for normalization, where m_ρ^2 is the mass of the rho-meson squared as the second lowest eigenvalue of the light-meson BLFQ. A similar study prior to [3,4,47] was conducted gaining minimally $\langle P_{\text{success}} \rangle > 1/3$ for specific cases based on BLFQ. The summary of the model’s limitations and strengths is listed in Table 1, id #5.

In [22–24], IBM-QE devices were used to code and simulate QFTh and QFTs in their proposed methods. The focus of these studies was on simulating condensed matter, spin Hamiltonian, potential wells, quantum circuits, and thermodynamic system models. These IBM-QE devices are employed to compute and compare SF transformation models for QFCMs, such as [7–12]. A QDF example from Section 1 is to implement a κ -based SF to a QDF transformation from Eq. (2) in a quantum circuit. This is achieved by observing multiple particle interactions and compute their level of entanglement within their QDF [7]. In [12], potential barriers are involved to perform a QFT compatible with an SF-to-QDF transformation, as discussed next.

From [12,13], Fig. 10(a) shows a single-step quantum circuit implemented for two qubits in case of QFT and its inverse QFT^{-1} using $[U]$, rotation gates, and $[H]$ gates. The equivalent labelled blocks have quantum circuits and gates shown for each corresponding image. Fig. 10(b) shows the implementation for a three-qubit simulation which includes the evolution of the Hamiltonian tunneling in a quantum multi-well between barriers.

	Direct Encoding			Compact Encoding		
	Classical Sampling	IBM Vigo	IBM Vigo, err. mit.	Classical Sampling	IBM Vigo	IBM Vigo, err. mit.
m_π^2 , no constant	0.48%	7.6%	7.5%	0.01%	11.6%	6.2%
m_π^2	0.90%	14.1%	14.0%	0.08%	12.7%	9.1%
$\langle r_m \rangle^2$, no constant	0.45%	6.6%	7.2%	0.43%	29.4%	7.1%
$\langle r_m \rangle^2$	0.65%	9.5%	10.4%	0.01%	6.4%	1.6%
f_π , no constant	0.05%	59.8%	59.0%	0.21%	29.2%	7.6%
f_π	0.02%	21.0%	20.7%	0.14%	13.0%	5.1%



© Images and table in Figs. 8 and 9 are extracted from the open access article, [3]

Fig. 9. Stepwise Hamiltonian plot based on fractional errors expressed as percentages in estimates of various observables calculated in the GS obtained. The results are reflected in the table above.

The results of low fidelity over a number of steps are apparent for a free particle, as shown in Fig. 10(a), which denotes more uncertainty in predictions in case of trapped in a single well. This, however, compared to QDF from [7], is predicted with $\langle P_{\text{success}} \rangle \geq 2/3$, given by Eq. (4), as a solution to such classical cases. Note that in [7], the QDF circuit partially benefits from Figs. 2 and 10 design to satisfy both QFT, its inverse QFT^{-1} , and [12], in its design and implementation of potential and kinetic energy operators.

In [7,8], a double-field computation (DFC) model, as a QF-LCA, simulates quantum observations on particle states and their distribution as lens products. These products are delivered through quantum lenses over distance d in a system, see Eq. (4). The implemented DFC algorithms make strong ST predictions in the system for both classical and quantum cases. The analyzed dataset with validated measurement outcomes in Table 2, predicted the system's final state relative to its input state. This study satisfies the conditions and solutions required for Eq. (1), by projecting the expected $\langle \mathfrak{M}(P) \rangle$'s from Eqs. (3)–(5). This required the inclusion of [12]'s simulation model, while improving its solution to simulate QFTs. This novel method is doubling the ST probability under a QFT, by implementing the QFT as a κ -based SF to a QDF transformation.

Earlier QFCMs discussed for [3–6,12–18,22–28], collectively satisfy Eqs. (1)–(5), but not on doubling the values of the ST probability space and its correlation to the system's pending ST or PT. The combination of model strengths, e.g., implementing a maximum fidelity strategy on performing a QDF transform with models [12,16], can achieve a UQFCM with high F 's in predicting strong $\langle \mathfrak{M}(P) \rangle$'s for a system. This requires a merging of common measurement parameters that all QFCMs share, as presented in Eq. (4) and Section 1.1.

The QDF model develops a method to implement a QF-LCA as a DFC method for two QDF systems [7–9]. The systematic review on the QF-LCA in simulating the two systems, is presented in [7,8]. The encoding and decoding layers of this model from Figs. 12 and 13, principally obey Fig. 3(a). The relationship between a quantum processor and registers on one side, and the classical decoder at the post-observation side, are the same as Fig. 3(a). However, the QDF model doubles the ST probability space by covering all quantum-classical information of the system state from a κ -based SF-to-QDF transformation, see Eqs. (2) and (4). The classical information is transmitted to the QDF from the SF using quantum gates. These gates are used to simulate energy operators in the QDF circuit from Fig. 13, similar to Fig. 10. These operators act on QDF qubits [7, p. 18]. Consequently, the number of processing steps is reduced between pairwise particle interactions and entanglement under a κ -based QDF transformation, see Fig. 12, Eqs. (2)–(4). This expected outcome shows a significant difference between QFCMs and the QDF that generates a consistent $\langle \mathfrak{M}(P) \rangle$'s in all cases of particle sampling and interaction in the system, see Fig. 13(b). The $\langle P_{\text{success}} \rangle$ correlates to ST probabilities of 2/3 and near values of 100%, making the QDF model reliable in uncertainty and error estimates under decoherence. Therefore, this model is less prone to

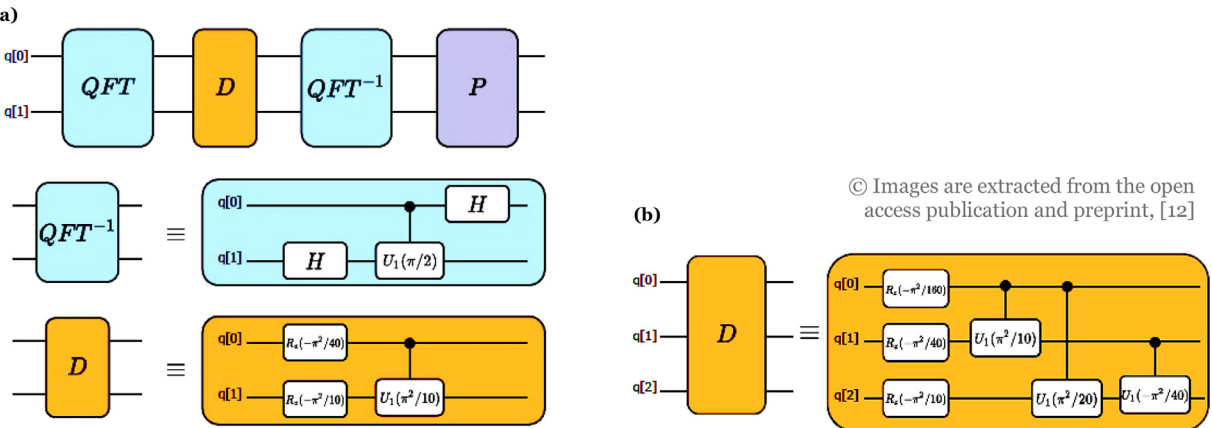


Fig. 10. Single-step quantum circuit performs a QFT and its inverse QFT^{-1} by implementing kinetic and potential energy operators using quantum gates. The theoretical and experimental results are shown in Fig. 11. (a) implements a step-well potential for a two-qubit system (upper Fig. 11 results). (b) is for a three-qubit system where the particle tunnels through barriers. The particle is confined in the well in a specific state, yet reaching great predictions of showing where it is situated after 10 steps (lower Fig. 11 results).

Table 4

Comparison of discussed models' ranging from the least to the most certain models in predicting system states relative to their measurement fidelity \mathcal{F} . Graphical Abstract gives a 3D representation of this graphical table. Each model is listed corresponding to their $P_{\text{distribute}}$ and P_{success} . The substitution, elimination and suggestion of a QFCM occurs at the model control stage (id #12 from Table 1) under the "decision layer" for the user or machine to decide as an IDS decision step. The model control includes QAI classification of states by an IDS decision for a UQFCM decision (outcome). After model control, a UQFCM decision is reached. Otherwise, the model control steps need to reiterate based on user's decision, given the IDS output from the previous step.

Measurement fidelity	Certainty range relative to a QFCM input	Condition	Distribution and success probability range output per model, ref. Table 1	Ref. Model(s)	Decision layer: user/machine-based
Max		Consistent in all cases for N interacting, free and/or trapped particles In elastic cases involving m qubits for the quantum register encoding the 1DG state. Kinetic and Potential energy operators perform QFT and QFT^{-1} between potential wells Error rate reduction and prediction in QFT _H , HEP, LQFT _H , single or double potential wells	<ul style="list-style-type: none"> $P_{\text{distribute}} \geq 2/3$ vs. $\leq 1/3$ $P_{\text{success}} \geq 2/3$ $P_{\text{distribute}} \geq 2/3$ vs. $\geq 1/3$ $P_{\text{success}} \geq 0.67 \approx 2/3$ $P_{\text{distribute}} > 0.5$ $P_{\text{distribution} \rightarrow \text{success}}$ is k-well dependent $P_{\text{distribute}} > 0.1$ $P_{\text{success} \rightarrow \text{distribute}}$ is dimension dependent (GS or ES uncertainty) 	[7-12, 38, 40, 52] + [18] + [12] + [3-5, 12-14, 17, 19, 23, 36-38, 47-54, 59, 60]	

error correction upon entanglement measurement via EE measures. The classical compiler and interpreter, mostly deal with quantum tunneling and teleportation scenarios in QDF simulations based on EE from [7], or see Eq. (4).

In summary, the QDF model presents measurements for predicting particle energy states. This model is used to determine an ST contributing to a system's PT on any scale, obtaining ST probabilities of $P \geq 2/3$. This is a significant statistical indicator of a thermal event expected to occur. In this system, an interaction length-based scalar κ , applied to a QF, transforms the field by a pairwise particle interaction via a QDF projection, see Eq. (2). The QDF model and its results on doubling the P have been evaluated in [7,11].

Graphical Table 4, lists QFCMs as input, and their $\langle \mathfrak{M}(P) \rangle$'s summary as the output to compare. The expected output, given the range of uncertainties in determining energy states based on a model's energy operators, e.g., [7-12], lists more certain QFCMs following their input method. This is shown in the graphical abstract as an 8-step QFC algorithm that achieves a UQFCM. An IDS classifies QFCM $\langle \mathfrak{M} \rangle$'s (outputs) using QAI. This includes supportive QFCMs' data from Table 1 delivered to the user by a QAI program to make a decision. This is achieved by concurrent processing of models' datasets relevant to a quantum experiment. As part of the model control process, one QFCM is chosen or switched to another, so to achieve maximum fidelity. In worst cases, the choice is a combination of QFCMs for the same range of fidelity as indicated in Table 4, 5th column. Then, reliable predictions of energy states can be made by implementing the 8 QFC algorithm steps. Further decisions are made to reroute energy paths to achieve a certain $\langle \mathfrak{M} \rangle$ efficiently. This expected outcome is exemplified in Section 4 as future work currently developed and validated by [7,11] results.

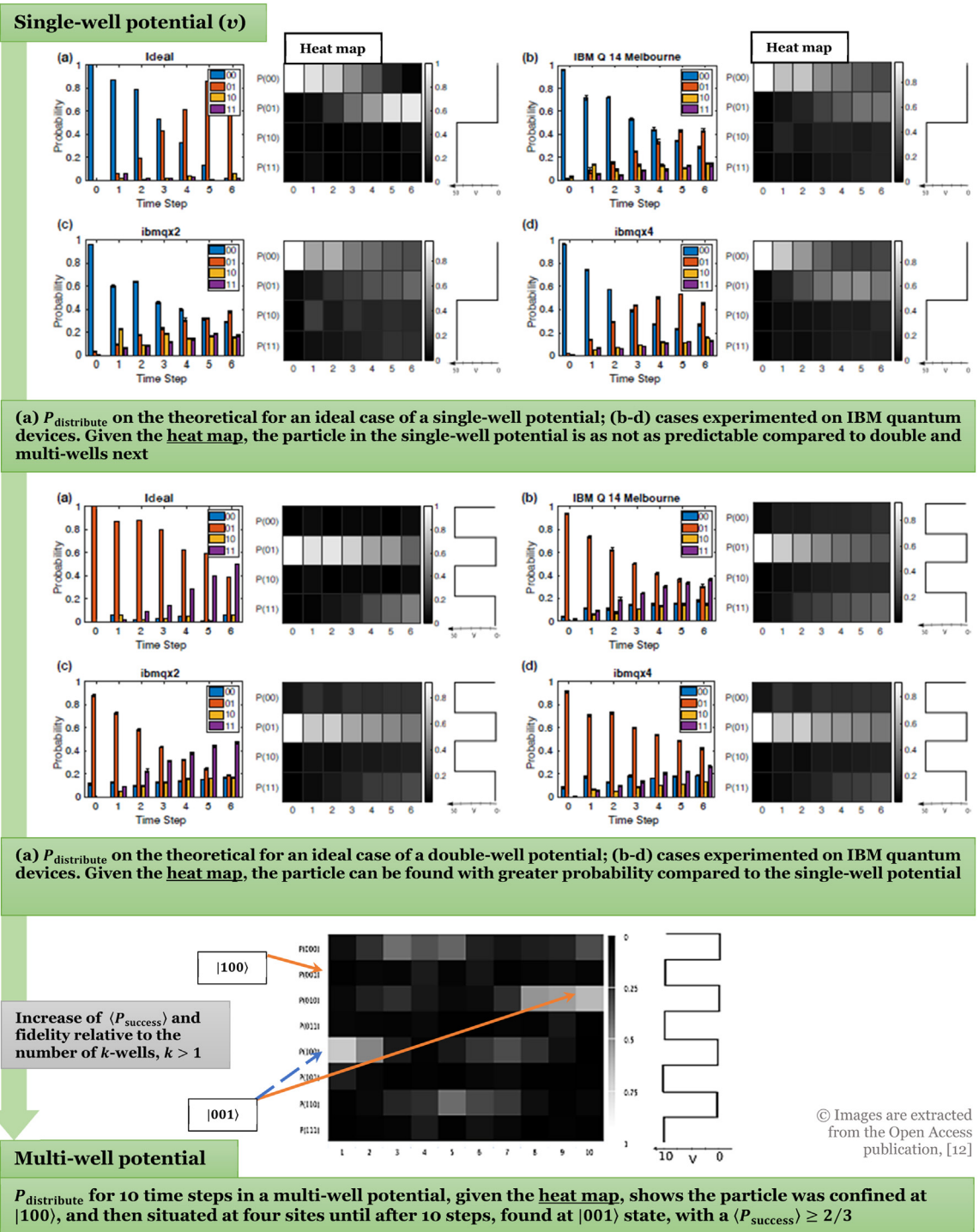


Fig. 11. Top-to-bottom) $P_{\text{distribute}}$ results are for single, double, and multi-well potentials, respectively. The probability of locating the particle and tunneling point in a specific state, increases to a significant degree, compared to top and middle well-potential cases (heat maps). These measurements were conducted with high fidelity satisfying the expected measurement outcome.

The UQFCM decision flow shows where model comparisons are made. QFCMs as input and their comparisons as output are controlled at the IDS step to decide whether a UQFCM outcome can be achieved. The selected models by IDS are [3-5,7-14,17-19,23,29-31,36,38,47-54,59,60]. The more its SMDB and encoders use classifiers from a QAI classification system, the more the IDS identifies a hybrid of classical and QFCM at decoding to make a strong prediction. QAI classifiers from all compared models, if

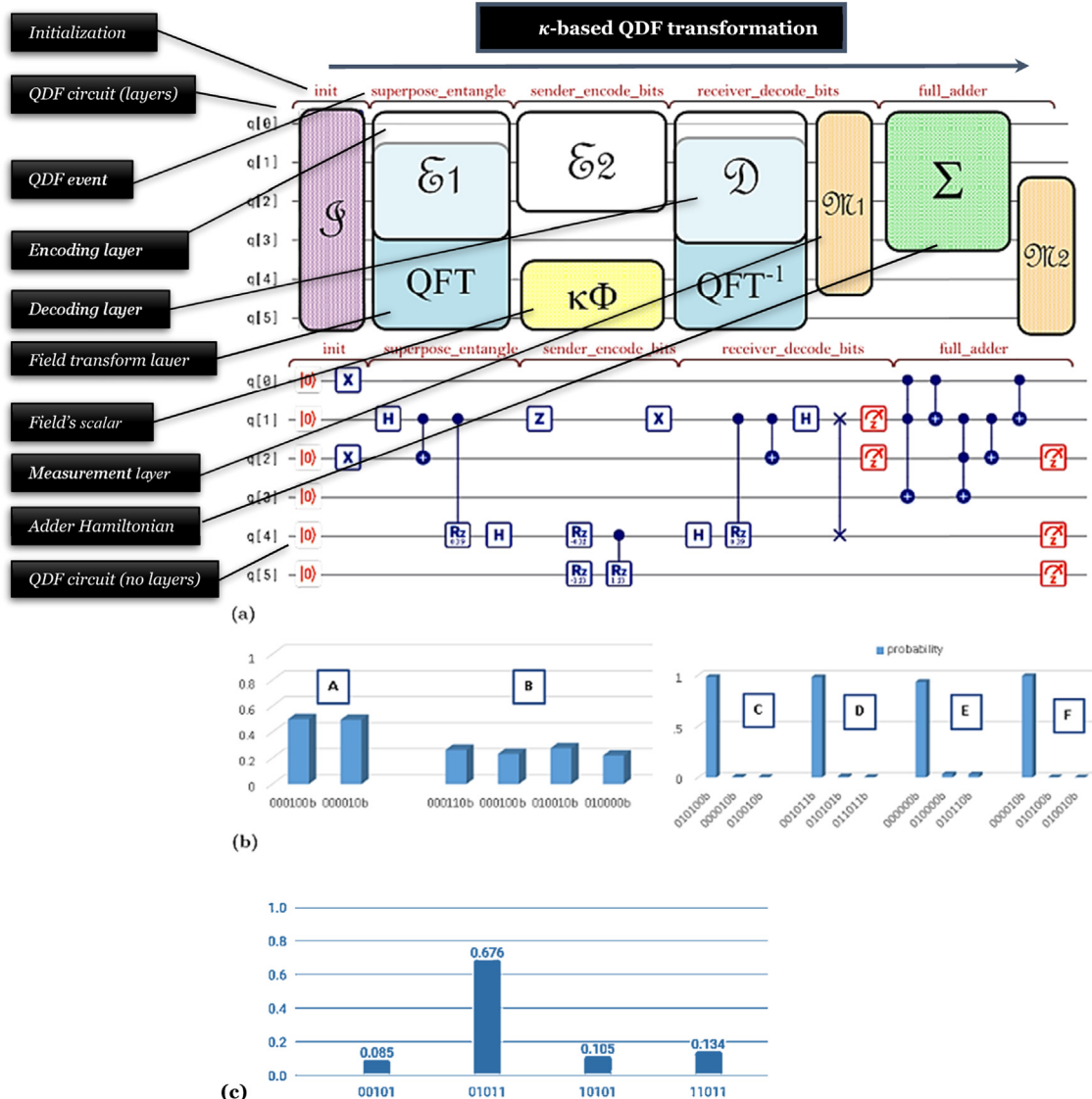


Fig. 12. QDF circuit components and I/O functions corresponding to Table 2 data; (a) Circuit I/O, initialization, encoding, decoding, addition and measurement layers as labelled and presented in [7]; (b) plots as labelled represent the same outcomes as labelled in [7, Fig. 5]. For instance, (b)B results denote a quantum outcome having the swap gate implemented compared to (b)A as discussed in [7, p. 28], by reconfiguring the circuit in its full adder function (sub-circuit) from `full_adder(1)` to run two iterations as `full_adder(2)`. The optimized outcome is (b)C-F as discussed on the same page in [7]. Examples of such circuit configurations for a specific measurement outcome and objective result are listed in Table 1; (c) QDF circuit reconfigured with no SWAP gate satisfies a classical outcome compatible with the QDF circuit configuration in upper Fig. 13. These results are represented under the two cases from Table 2, and the graph from Fig. 13(b).

not suitable for a desired Hamiltonian, can then access open-source datasets to propose a QFCM added to the QFCM list for more comparisons, see Section 1.2. A hybrid model can then lead to a UQFCM after simulating the model's $\langle \mathfrak{M} \rangle$.

Future work with the graphical abstract and conclusions, answers the 5th review question on:

- the possibility to achieve a UQFCM in making a strong prediction of a system state using QAI, and for the 6th review question to have:
- a trained QFCM embedded in other simulators to simulate physics and make strong predictions.

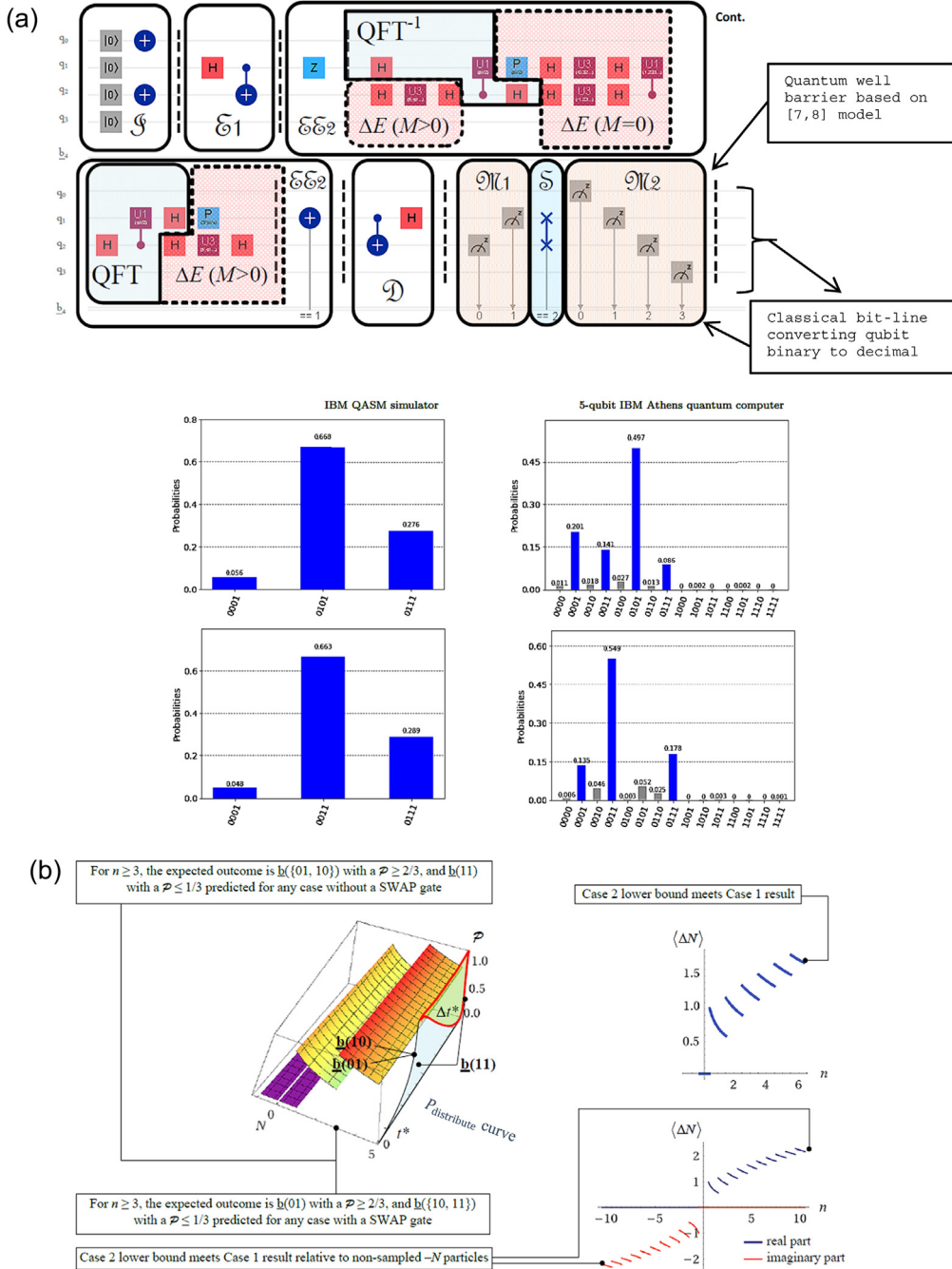


Fig. 13. Upper figure a) is the QDF circuit design compatible with QFT and QFT^{-1} design from Fig. 10 or its equivalent QDF circuit in Fig. 12(a), showing a QDF transformation via scalar κ in the circuit, Eq. (2). Here, the energy operators extend to include the magnetic state between pairwise spins of the spin Hamiltonian denoted by M measured from the energy interval function $\Delta E(M \geq 0)$ between a particle pair. The algorithm encodes (ϵ) or decodes (\mathcal{D}) their quantum states as discussed in [7]. Lower figure a) The histograms show different scenarios on double-field sites and their complements. For example, if P is $1/3$, the complement is predicted with a P of $2/3$, appearing in state 10 as opposed to 01 in the qubit setup of 0101 and 0011 in the circuit. This is where particles exchange quantum information (QI) within the QDF as simulated using IBM quantum computers. The entanglement between particle pairs is determined by measuring (\mathfrak{M}), and its EE during a κ -based SF-to-QDF transformation in this circuit. Bottom figure b) EE scaling graph of the QDF circuit is the left graph b) which illustrates the phase shift region of pairwise particle interactions. From their $P_{\text{distribute}}$, values of $P > 2/3$ are predicted as classical information (states) from the particles' QI.. This is denoted by the function converting the pairwise qubit state to decimal. For example, the constant trend with probability $P \leq 1/3$ is for $b(11) = 3$ in decimal, and is the complement of $b(01) = 1$ and $b(10) = 2$ in all cases of $n \geq 3$ interacting particles (right graph b). Implementing the circuit with a SWAP gate vs. a no SWAP gate, projects a probability trend of $P \geq 2/3$.

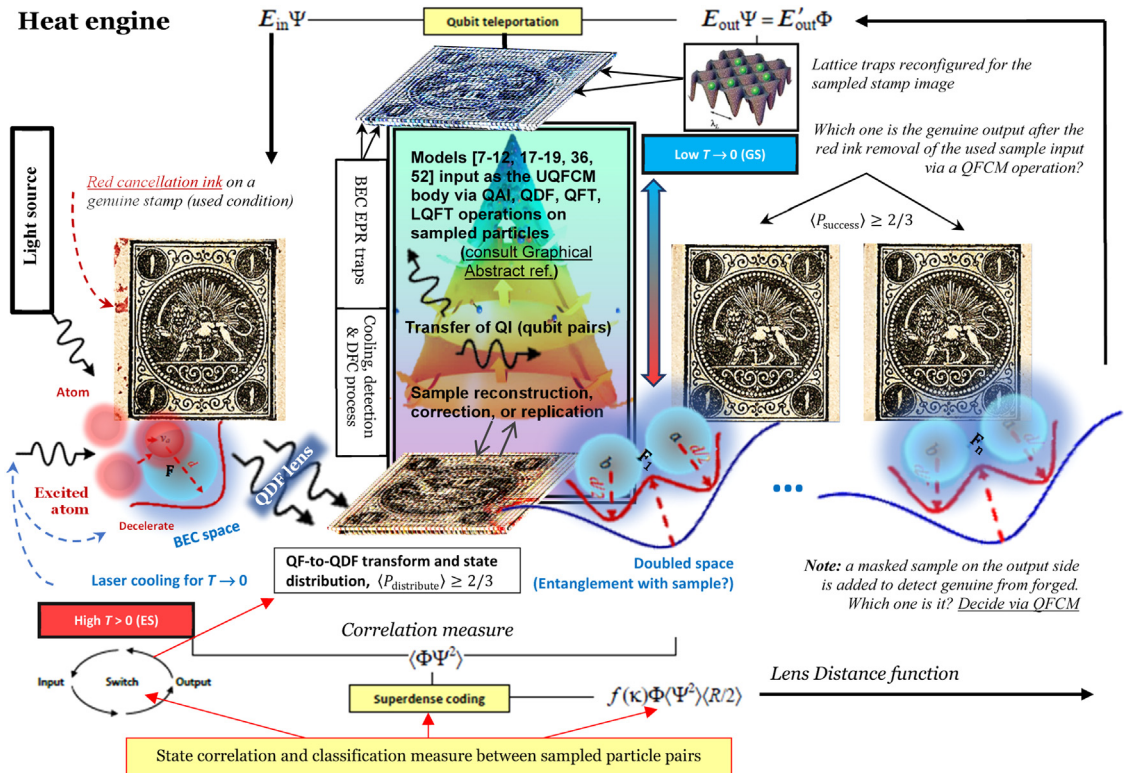


Fig. 14. Selected QFCMs operating on particle samples. **Left)** on the energy input side $E_{in}\Psi$ denotes an atom sample of a used Persian stamp (imperforated): Coat of arms (Lion & Sun with sword), black 1Chahi (currency unit at the time) with English numeral under the lion's belly printed in 1876. Catalog value of a mint condition is worth 1K USD compared to forged types of 10^+ USD, and a used genuine is est. 250^+ USD [35]. **Left-to-right)** events from the DFC concept [8] obey Fig. 15 Hamiltonian model. It detects spins between sample's input state and output state by measuring their QF's correlation function of $\langle\Phi\Psi\rangle$. A three-field correlation $\langle\Phi\Psi^2\rangle$ is measured between input-output paired particles of average position field $\langle\Psi^2\rangle$, and a photon of average momentum field $\langle\Phi\rangle$. This is distributed via superdense coding between the GS on a BEC scale, and ES of the sampled atom, paired with the photon from a light source (laser beam) in the QDF heat engine. **Middle and bottom)** The flow of events simulates the correlation measure and state classification by switching QFCM algorithms between sampled particle pairs within a doubled probability space from a κ -based SF-to-QDF transformation, Eqs. (2)–(4). The input-to-output particle samples and their states are classified according to Fig. 15. The flow is a sample's input of a GS and ES \rightarrow {QDF + QFCM operations + QAI} \rightarrow output sample. Entanglement between sample's ES and GS regimes is then determined and classified. **Right-to-left)** Entanglement is determined between constructed samples e.g., forgery (whether on the input side or output side) and genuine. The greater their fidelity of states, the more identical to the input. If the input is forged, the output is as well, if not, it is either a newly-constructed one, altered, or genuine. Then, the E_{in} and E_{out} cycle reiterates.

4. Future work

This section explores some examples that can hypothetically employ QFCMs, for a UQFCM, from Table 4.

4.1. Measurement examples and algorithm

From the measurement-based parameters of the reviewed models' strengths and limitations in Tables 1, 2, and 4, given their $\langle\mathfrak{M}\rangle$'s as $\langle\mathfrak{M}(P)\rangle$'s and $\langle\mathfrak{M}(F)\rangle$'s, the following method employs QFCMs with high $\langle\mathfrak{M}\rangle$'s using an IDS. In this case, quantum tunneling and qubit teleportation are exemplified for this choice to satisfy the $\langle\mathfrak{M}\rangle$'s from e.g., [7-12,40,52] models. To propose a UQFCM based on the IDS, a QFCM input and an expected output are evaluated as $\langle\mathfrak{M}\rangle$'s with high F . Alternatively, a combination of QFCMs is made to deliver a reliable and efficient outcome for predicting an experiment.

In the case of qubit teleportation, a QAI algorithm is employed to determine suitable QFCMs in proposing a UQFCM. Quantum AI algorithms employed by QFCMs, e.g., combined with the DFC model [7,8], and quantum-classical hybrid models [42–44], can achieve high fidelities in classical and QF measurements on matter. For instance, consider fields involving security, monetary losses and antiquities of static (fixed) fields. A QDF of a DFC model involving solid matter fields, based on QFT_h, can duplicate classical static fields of e.g., a genuine postal stamp [34], or a copy of a painting claiming to be the original from centuries ago.

Fig. 14 shows a QFCM identifying a forged stamp from genuine. This is achieved by replicating the 2nd field of a QDF transformed from a used stamp single-field F , as $\{F_1, \dots, F_n\}$ on a genuine against a forged stamp (masked). The QDF signature replicates and validates the exact material (atoms) used for the forged against the genuine (used, unused, or mint) stamps. This is by observing

particle field entanglement from their QDF lens function (*lens distance and correlation function*) in a QDF heat engine [8]. This engine performs a PT of particles sampled from the original material (input) compared to the forged or replicated (output). The output must indicate one of these states: stamp is *altered* by removing the cancellation ink, or, *unaltered* by adding a mint one as a masked sample output to compare and determine their QF's level of entanglement. If a negative correlation is observed, the forged from the original is determined. The closer the lens distance d , Eq. (4), between the two samples [7, Eq. (9)], the closer to be the original to their issued date and condition. The entanglement between the input and output samples is determined based on EE measure [7], see Figs. 12 and 13. In Fig. 14, the cycle of qubit teleportation to/from its *reverse protocol* i.e., *superdense coding* as a QDF circuit, is to satisfy an energy condition for a reversible thermodynamic model [7, pp. 11–13], [52,58]. This is to determine the entangled state between the energy input and energy output side (see circuit code in [7]). The spin Hamiltonian is shown in Fig. 15 for an entangling Hamiltonian. Energy (state) differences are shown corresponding to temperature T (in kelvins) in a κ -based SF-to-QDF transformation, see Eq. (2).

To reconstruct or replicate particle pair samples, the correlation function between three fields $\langle \Phi\Psi^2 \rangle$ must be measured i.e., observing a double-field of a particle pair and its interacting photon field. This requires 2D to N -dimensional lattice sites reconfigured for the sampled stamp image (a cliché), via BEC or BEC EPR traps, see Fig. 15, or EE scaling from [7]. This is a costly construction process to perform an entangling Hamiltonian between the CPT and QPT regimes in determining entanglement from other particle states. However, once these traps are created, unlimited sampling, forging, identifying and classification of any sample can be made, as a gainful strategy. For instance, balancing out the initial costs and benefit economically on correlation measure, reconstruction, and replication services, is a matter of investment towards information science, forensics, medicine, security, arts, etc. Correlation test results can then be input to a QAI program to classify and examine more samples about fabricated documents, signatures, banknotes, reconstruction of destroyed evidence, DNA, etc. This is one example out of many future works that a QDF model as QF-LCA, combined with other QFCMs relative to a UQFCM, can benefit users operating in a quantum environment.

Gen-forge QFCM algorithm: compares forgery against genuine samples \pm transformation

Input: target correlation function between sampled particle fields as the κ -based SF or QDF function

Input (external): target sample's macro features from known expert databases about forged and genuine samples

Output: print correlation between particle samples on the quantum scale (smallest scale representing the classical sample or object). This shows the level of authenticity of each sample.

START

1. INPUT a QFT model for a κ -based SF or QDF transform as an option: Table 1 models or [7-12,17-19,36].

a. Input sample to read its structure via heat engine components (photonic probes and sensors) and storage access #*Engine components are simulated as part of the software comparing collected/registered data through storage*.

b. Input (external) sample to read and compare for input sample's macro features # *Macro features are classical, exemplified in Fig. 16 to compare sample's appearance based on original print cliché of A-D types*

c. Measure system events by targeting field function on sample particles. # *This produces P's event data on the sample's particle state*.

d. IF data comparison and classification of QFCM is based on $\langle P_{\text{distribute}} \rangle \geq \frac{2}{3}$, GOTO step 3,

e. ELSE Transform field(s) of sample particles via heat engine.

2. Compare and classify P 's of sample particles:

a. P 's between macro features and determine strong P 's as $\langle P_{\text{success}} \rangle \geq \frac{2}{3}$ from $\langle P_{\text{distribute}} \rangle \geq \frac{2}{3}$

b. P 's that are not strong P 's as $\langle P' \rangle$ compared to step 2.a., to determine degrees of authenticity based on $\langle P_{\text{success}} \rangle$.

3. PRINT OUT or store results, # *This is stored and displayed as a chart, here as a *.csv or *.xls file format*

4. Process experiment results.

a. IF sample genuine, GOTO step 6,

b. ELSE IF sample forged or transformed

i. Decide YES, report forged or transformed, GOTO step 6.

ii. Decide NO, transform sample to transform forged to genuine, GOTO step 5.

5. RUN QAI/AI program: # This step executes a classical and quantum hybrid AI program to transform the sample

a. INPUT probability and fidelity results on expected measurements relative to YES or NO decision for/against achieving accurate outcomes of steps 4.a and 4.b.

b. PRINT OUT distance-based classification of results from specific QFCMs [7-11] employing methods like [30]. Reiterate step 1 with step 1.e enabled.

6. Publish correlation function results between samples as a datasets or report as unaltered or transformed sample(s).

The following two steps are optional to code for optimization purposes in targeting strong correlation results

7. Validate results or test further to conclude a successful experiment as a UQFCM on this sample.

8. Decide algorithm's candidacy for a UQFCM,

a. IF YES, PRINT OUT algorithm meets a UQFCM expected measurement outcomes and fidelity

b. ELSE revisit steps 1 to 7, revise code for step 8.a.

HALT

The flow of events in Fig. 16 is simulated by a QFCM algorithm that proposes the sampling, measuring, reconstruction and replication of I/O data from sampled particles in a heat engine, see Fig. 14. The algorithm is written in a pseudocode form with supplementary comments presented after a # notation, like in Python, or QASM code written for QInspire or IBM-QE simulators [33,50]. The data must represent physical values (particle type, energy, momentum, position, density, frequency, etc.), as well as probability values for a classical or quantum state, GS, ES, ST, PT, etc. The analysis and classification are made after the input data as internal (from the heat engine) or external (from a database of forged and genuine samples [34,35]). Classifying these data through code [7], requires the sampling of the physical state of sampled particles, for or against genuine samples (particles) taken from the stamps under observation in a lab. Sensors or probes of photons (aka photonic probes [7-11]) are used, as shown in Figs. 14–16, to

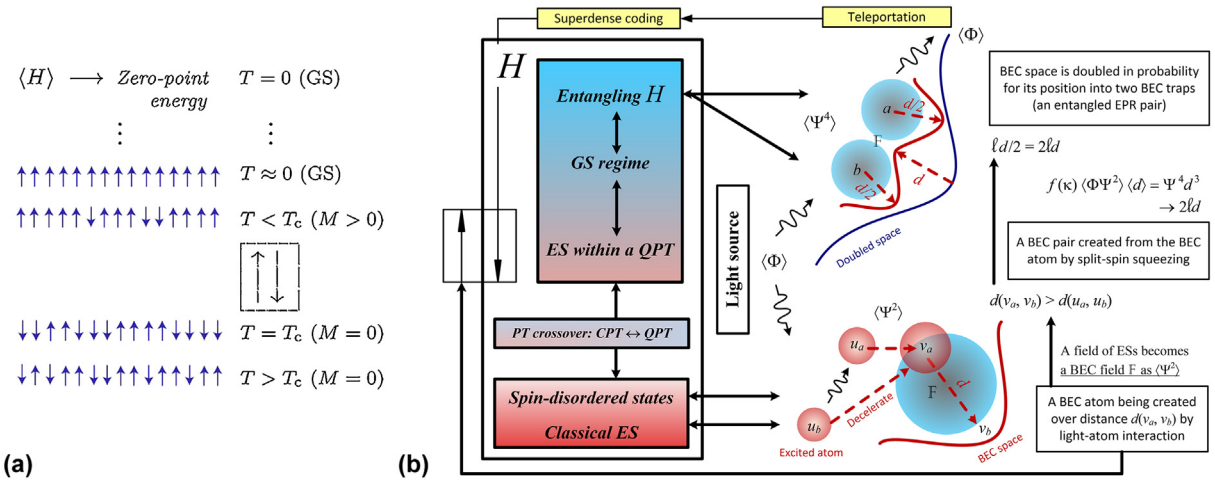


Fig. 15. Spin Hamiltonian revisited from [7,8] as a DFC algorithm; (a, b) correspond to thermodynamic events in Fig. 14; (a) Spin-ordering simulation for the Ising model, as temperature increases (top-to-bottom) magnetization M changes to a zero net value. The correlation length increases when temperature is decreased (ordered spins), and diverges at critical temperature T_c . If the external field is absent, there is still $M = 0$; (b) The cyclic production of BECs via atom-light interactions with an expected spin order in (a), is to create BEC EPR pairs in an entangling Hamiltonian, scaling H between ES and GS regimes. A pair's space in probability doubles in a correlated QDF with photon field by their function $\langle \Phi \Psi^2 \rangle$, as opposed to a disordered non-BEC space. Teleportation is performed after doubling, as the classical states are decoded by sharing the EPR state via superdense coding [7].

store, access, read/write data. Data writing is in document form for reporting results of genuine vs. forgery types. In Fig. 16, this is presented as a spreadsheet chart from step 3 of the algorithm. On the other hand, data writing and sample transformation can be explicitly instructed by the model or user's choice based on evaluating $\langle P_{\text{distribute}} \rangle$ between steps 2 and 5. This choice, after decision step 4, can result into methods delivering ink or any other required material from an atomic force microscopic (AFM) tip for the stamp [36, pp. 2–5]. This includes the stamp's gum, fabric, and its structural reconstruction. The AFM tip and inkjet printing, or other micro-to-nano printing methods, including their advantages and disadvantages, are discussed in [36]. The tip size is attributed to the micro-/nano-scale printing technology. The inks used can consist of small molecules, polymers, DNA, proteins, nanoparticles and peptides, directly transferred to the substrate with accuracy on a sub-nanometer scale [36]. This includes printing micro-/nano-scale sensors and circuits.

Fig. 16 shows a used rare (genuine) stamp for comparison to authenticate the unused rare stamp (its upper left) based on features and Type D Cliché description in re-engraving the 1 Toman issue in 1878. Same blue paper and violet print, requires a good match with A-D features, mainly A, B and D, which fit for the unused stamp in question. If the stamp's back is also reconstructed, as shown by 3D printing, after authentication (?), step 2.b of Gen-forge, it will be one of the rarest unused stamps recorded in history in excellent condition (7 unused copies are known [34]). Can this be one of the lost or hidden ones added, or, a good forgery?

For the rare sample determination, data results at the 'register & print' step 3, mixes the sampled example measurement results based on feature comparisons database from step 1 as 'read sample'. The assumption is 100% forged, yet, with the possibility of transformed/altered to be $\langle P_{\text{success}} \rangle \geq 2/3$ genuine. This is tested by employing predictive transformation models (Fig. 14) with strong prediction outcomes, e.g., QDF and QFT from Table 1. The complement of the output, is the assumption for the genuine type as the input, which is

$$\text{Input } (\langle P' \rangle) = 1 - 2/3 = 1/3 \text{ for } P(\text{gen}),$$

and the difference, or Δ , is

$$\text{Output } (\Delta P) = [1 \text{ for } P(\text{forg}) - 1/3 \text{ for } P(\text{gen})] = 2/3 \text{ transformed, genuine, or mixed,}$$

given the sum of sample tests run by the selected QFCMs. Once classified and printed as a report, at step 5, the QAI algorithm weighs the data for either an SF or QDF transformation from Eq. (2). This is to determine whether reconstructing the damaged parts are needed, or transform the sample from forged to genuine, or conduct further detection as part of the experiment. Finally, a report is printed and the program ends (HALT).

After discerning the forged from genuine stamp(s), a physical reconstruction or replication to improve the value of a damaged stamp/gum to a mint or a duplicate with a high USD value, a 3D printer can be used, Fig. 16. Although this is forging with perfection, the printing process can be useful in reconstructing damaged or lost data in science and industry, as discussed earlier. This leads to whether the algorithm can be a good choice to represent a UQFCM, given the facts of its future scope to improve QFCM limitations and strengths.

Among QFCMs from Tables 1 and 4, AQO [48] and AQOpt [51,52], can be explored to employ and adapt the Gen-forge algorithm to satisfy objectives 3 and 4 from Section 1.1. For example, consider using photons in the heat engine in a disordered state over

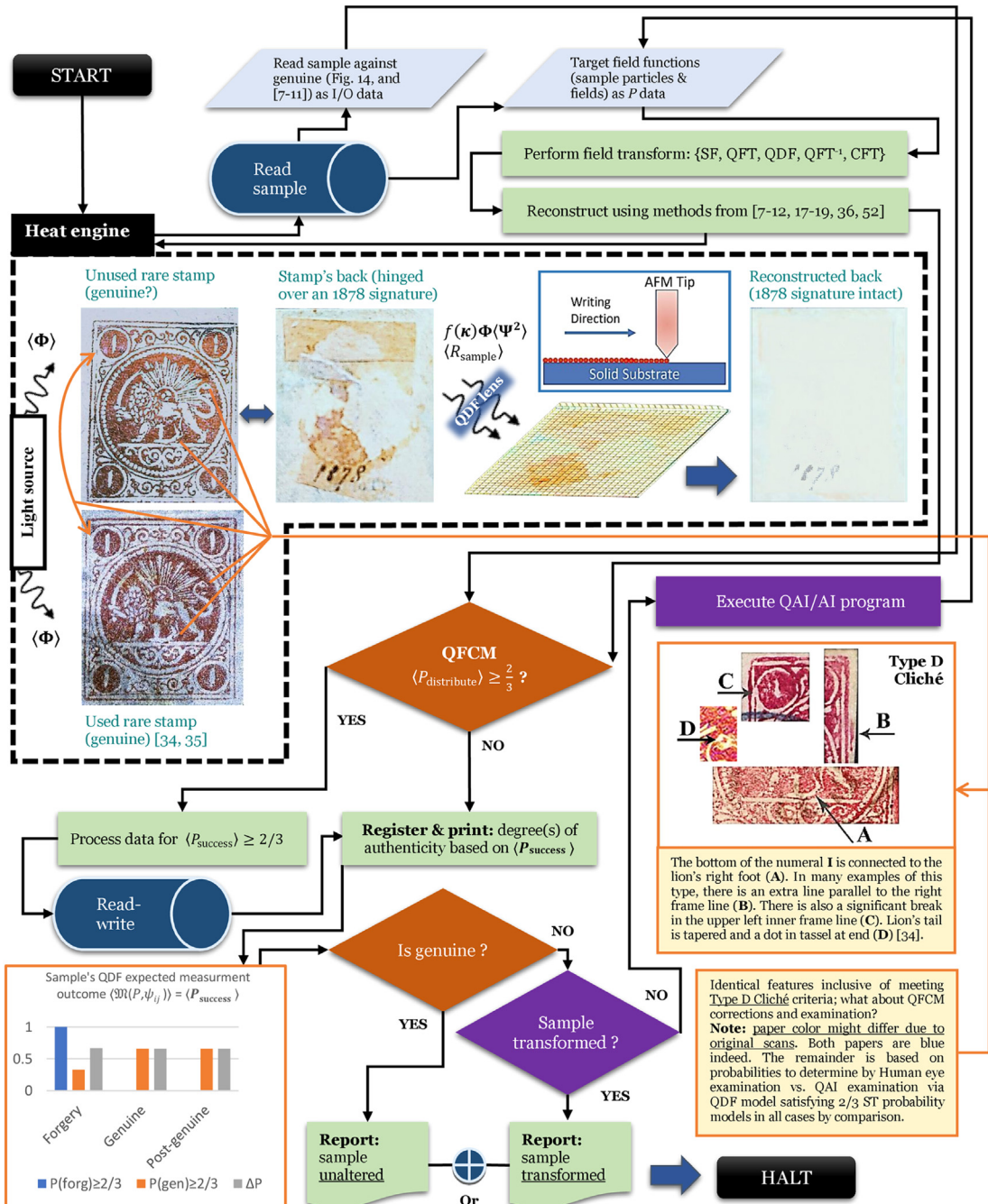


Fig. 16. Further replication uses a micro-/nano-scale printer [36] to rebuild and replicate a forged against a genuine stamp. This stamp of 1 Toman (= 200 Chahis = 200 stamps from Fig. 14), as the highest denomination at the time, printed on blue paper with reddish bronze or violet print of the lion. If genuine, is worth around 80K USD according to the 2020 catalog value [34]. Since there is barely 7 of the unused copies (with damaged gum) recorded, a mint condition can be very few. This is the author's (P. B. A.) own stamp purchased on e-Bay auction, given the knowledge that it could be genuine, since it has a history of being inherited from a Royal British officer who served in Persia in 1878, to its seller. To certify its authenticity, the author and expert of [34] can evaluate against an identical type or genuine. This evaluation is based on paper (blue), appearance (as shown for this type printed from Type D cliché), and errors in the original print which was printed from the original cliché. Regardless of the outcome, Gen-forge algorithm steps are executed to compare between the outside expert opinion, Gen-forge user's opinion, and QAI output. Reconstruction can be made to make a perfect forged, or genuine, or alter it by transforming the forged type to a genuine type. This is by feeding the information and material needed to the 3D printer on nano (or macro) scale, as part of the heat engine. After printing, for more reconstruction, replication and comparisons, Fig. 14 can be revisited by restarting the Gen-forge algorithm.

a communication channel between the input and output particles in Fig. 14. The AQOpt method is during the sampling process of pairwise particles between the engine's output side as a result of an SF, QFT, or QDF transformation, and the engine's input side. The input side has photons emitting from the light source onto the pairwise particle samples. The method to measure EE in this case, is shuffling the photons and preserve information between steps 1.d and 3, while transformation occurs at step 1.e. This is assuming the user or QAI program have decided to transform the sample at steps 4 and 5. Further analysis and validation between the selection of such models, according to step 1, and Table 4, can be made according to steps 6–8 of the Gen-forge algorithm.

The following section summarizes the mapping of Gen-forge's steps 6–8 results to other QFCM candidates. This produces (\pm) strong correlation results for a UQFCM. Compatibly, the results meet step 8 of the graphical abstract, so as the other Gen-forge's steps on a smaller scale for achieving a UQFCM.

4.2. Future scope

From Figs. 14–16, a QFCM algorithm was proposed as a Gen-forge simulator, where similar algorithms can be coded obeying its state decision process. These algorithms need to conform to the steps presented in the graphical abstract for a UQFCM, relative to Table 1 and 4 model control, processes, datasets and expected measurement outcomes. The scope of the heat engine is to physically sample, measure, reconstruct, and replicate I/O data. However, this simulator should project results based on the data feed from online past/real-time datasets published by actual labs. In the hypothetical example, the simulator's objective was to reconstruct particle paths of a damaged postal stamp, compare it, and examine its authenticity. This involved a QAI algorithm to distinguish genuine samples from fabricated. Other examples are, examining documents under controlled conditions at a forensics lab, so to predict events related to a crime scene after data reconstruction. The data must represent physical values as particle type, energy, momentum, position, density, frequency, etc., and probability values for classical or quantum state transitions, GS, ES, PT, etc.

DNA sampling, printing parts of the DNA code as strands of molecules to reprogram against e.g., cancer cells, or a virus, can be achieved when high measurement fidelity and expected outcomes are made. This is to find the best model candidate based on an algorithm step that can meet the UQFCM's expected measurement standard against a QFCM limitation, as specified in Gen-forge's steps 6–8.

QFCMs' future scope is focused on simulating systems based on the review of QFCMs that predict system states reliably. Among which are to reliably predict HEP events in experiments conducted at CERN, where LHC datasets can be used to make predictive advances of LHC data events. The main challenge is to address each model's limitations through monitoring its $\langle \mathfrak{M} \rangle$'s, relative to events' dataset input, as identified in Table 1. For publishing data-driven prediction results, a UQFCM output has to represent a QFT describing a system event. For example, in condensed matter physics, a combustion or refrigeration event is predicted, compared to jet engines at industrial scales impacting the environment. A constant requirement for a QFCM as a UQFCM, is to perform a high F in predictions for $\langle \mathfrak{M} \rangle$'s. This is needed for predicting events in experiments, as their datasets expand and updated. The other challenge is reconfiguring code for specific quantum circuits when a QFCM code is executed on e.g., an IBM-QE device, compared to QX simulators running on a classical supercomputer. Such challenges are addressed by simulating events in a hybrid quantum-classical simulator. The application of this model was discussed, hypothetically, to make strong predictions of motion and STs real-time, e.g., for human-assisted self-driving vehicles. In this model, the external QF of a body on road is associated to the internal QF of the vehicle to measure their particle field entanglement based on an EE readout. Reacting and choosing the right route with a high P_{success} is by doubling the paired QFs probability space by a QDF model. The classical system then reliably actuates the decision command after prediction by a QAI program. As a result, a UQFCM with strong predictions of STs, simulates energy paths and then reroute them to choose the most efficient path. For example, in a jet engine, make certain particles not participating in a thermal event, to participate, so to increase efficiency. This leads to a UQFCM with a strong system state prediction, in order to achieve a desired Hamiltonian.

5. Conclusion

Fundamental questions about simulating the observable universe on classical and quantum scales were addressed in this review. Among which was evaluating quantum field (QF) computation models (QFCMs) on quantum computers to simulate a physical system. The selection of a QFCM was based on comparing QFCMs' strengths and limitations in measurement parameters that measure a system state. This includes QFCMs expected measurement outcomes, $\langle \mathfrak{M} \rangle$'s, to predict system events based on the expected success probability $\langle P_{\text{success}} \rangle$ over state transitions as system events. This probability is yielded from the probability distribution of particle states in the system, $P_{\text{distribute}}$. The more consistent a QFCM in simulating the $\langle \mathfrak{M} \rangle$'s for an experiment, the greater the model's measurement fidelity $F > 0$. QFCMs were selected based on the F of states, their error rate reduction, and P_{success} . QFCMs, such as LQFT, HNT, CFT, QFT, BLFQ, 1DG of QFT, AQO, AQOpt, QDF, for HEP and BEC, were compared in their measurement strengths and limitations. From all listed models, their F 's were averaged to $\langle \mathfrak{M}(F) \rangle \geq 7/5$, denoting 7 QFCMs are optimal compared to 5 less optimal QFCMs in predicting events consistently with success. Measurement limitations were addressed by combining measurement parameters to satisfy maximum fidelity, $\max F \rightarrow \infty$, for a select set of QFCMs. Measurement data on quantum states are decoded as classical states. Prediction results come from sharing P_{success} 's in classifying states. This is by focusing the $P_{\text{distribute}}$ of states from those QFCMs with $\max F$, such as QDF, compared to stochastic types observed within a set of quantum states, as in the LQFT model. This proposed the development of a universal QFCM (UQFCM) to simulate systems with strong prediction results.

Model limitations can be controlled by maximizing model strengths through a model control process. For example, a UQFCM reduces the error rate or uncertainty of a system state measure, given $\langle P_{\text{success}} \rangle \geq 2/3$ of a selected QDF model as a strong predictor of the system's final state. This priority is given by eliminating QFCMs with low fidelity $F \rightarrow 0$ in measurement data that are input

by an intelligent decision simulator (IDS). Examples of low fidelity would be in quantum tunneling cases where data loss is expected for single and double potential wells under a QF transformation. However, the higher the number of potential wells, the greater the $\langle P_{\text{success}} \rangle$ and F between energy states entangled to preserve low information loss. With this quantum information (qubits), a strong prediction can be made on where the particle will appear in a specific site. The goal was to keep those QFCMs with high F 's by the IDS selection. When a certain quantum condition arises, regardless of missing parameters, the selected QFCM must still achieve strong predictions. As part of the IDS, all QFCMs remain to input for a quantum AI (QAI) algorithm. A QAI program classifies, decides, and suggests a QFCM to make a strong prediction of an event for the system.

QFCMs' future scope is focused on simulating systems and predict their events reliably. One major challenge is to address each model's limitations through monitoring its $\langle \mathfrak{M} \rangle$'s relative to events dataset input. For publishing data-driven prediction results, a UQFCM output has to represent a QFT describing a system event. By addressing model limitations on $\langle P_{\text{success}} \rangle$ and $\langle \mathfrak{M}(F) \rangle$ results, a high F in model predictions becomes a constant requirement to perform as a UQFCM for predicting events. The other challenge is reconfiguring code for quantum circuits when a QFCM code is executed on quantum devices compared to classical. Such challenges were addressed by simulating in a hybrid quantum-classical simulator. Among the presented examples, the application of this model was discussed for kinetic and potential systems/bodies. In this model, the external QF of a system is associated to the internal QF of the system to measure their particle field entanglement level. To choose the correct efficient route with a high P_{success} , is by doubling the paired QFs probability space via a QDF model. The classical system, then reliably actuates the decision command after prediction by a QAI program. As a result, a UQFCM makes a strong prediction by simulating energy paths, rerouting them to choose the shortest, most efficient and correct path. The reconstruction of particle paths of a damaged evidence e.g., DNA, collectables, ID's, etc., was also discussed involving QAI to discern original samples from fabricated as other QFCM's viable products to operate and deliver service to its users.

Finally, a UQFCM gives a more focused method of measuring physical systems by presenting a unified solution to their prediction problems. The study and development of technologies from the physical world on an industrial scale can be cost effective when a UQFCM is achieved, as it improves system design, state control and performance of those technologies.

Ethics statements

No human participant was involved in the review's data acquisition and analysis.

Supplementary material

An indication of how to develop a universal QFCM from QFCMs that satisfy a maximum measurement fidelity is e.g., [10], with a code example and dataset to use as discussed and validated via [7].

Funding

This work was supported by the [University of Victoria](#), Canada, for financial support, award no. [V00766282, 2015-2023](#).

Declaration of Competing Interest

The authors declare that they have no known competing financial interests or personal relationships that could have appeared to influence the work reported in this paper.

CRediT authorship contribution statement

Philip Baback Alipour: Conceptualization, Methodology, Investigation, Writing – original draft, Visualization, Formal analysis, Resources, Funding acquisition, Project administration, Validation, Writing – review & editing. **Thomas Aaron Gulliver:** Supervision, Resources, Validation, Funding acquisition, Project administration, Writing – review & editing.

Data availability

Online reference to data is provided within this work.

Acknowledgments

P. B. A. and T. A. G. thank Dr. T. Lu for comments on the scalar field models, dimensions and photonics on the QDF model development, Dr. M. Laca for comments on QDF model's four measurement variables [7–11], Dr. N. Neumann remarks on QAI classifiers [29,30], and the late Dr. F. Diacu for comment on phase transitions to parameterize their quantum probabilities in the QDF model [7–11]. All of which, in this review, were compared to QFT models to propose and develop a universal QFCM.

References

- [1] R.P. Feynman, Six Easy Pieces: Essentials of Physics by its Most Brilliant Teacher, 4th edition, 2011 Basic BooksChaps. 2-6. Or see <https://www.pdfdrive.com/six-easy-pieces-essentials-of-physics-explained-by-its-most-brilliant-teacher-e156765078.html> (1994) and The Feynman Lectures on Physics: Basic Physics (caltech.edu) 1 (1963) Chap. 2 [accessed Feb. 5, 2023].
- [2] F. Mandl, G. Shaw, in: *Quantum Field Theory*, Wiley Press UK, 2010, pp. 1–3. Chaps..
- [3] M. Kreshchuk, S. Jia, W.M. Kirby, G. Goldstein, J.P. Vary, P.J. Love, Light-front field theory on current quantum computers, *Entropy* 23 (5) (2021) 597, doi:[10.3390/e23050597](https://doi.org/10.3390/e23050597).
- [4] M. Kreshchuk, W.M. Kirby, G. Goldstein, H. Beauchemin, P.J. Love, Quantum simulation of quantum field theory in the light-front formulation, *Phys. Rev. A* 105 (2022) 032418, doi:[10.1103/PhysRevA.105.032418](https://doi.org/10.1103/PhysRevA.105.032418).
- [5] A. Avkhadiev, P.E. Shanahan, R.D. Young, Strategies for quantum-optimized construction of interpolating operators in classical simulations of lattice quantum field theories, *High Energy Phys. - Latt.* (2022) (hep-lat) arXiv.org, doi:[10.48550/arXiv.2209.01209](https://doi.org/10.48550/arXiv.2209.01209).
- [6] A.H. Moosavian, S. Jordan, Faster quantum algorithm to simulate fermionic quantum field theory, *Phys. Rev. A* 98 (2018) 012332, doi:[10.1103/PhysRevA.98.012332](https://doi.org/10.1103/PhysRevA.98.012332).
- [7] P.B. Alipour, T.A. Gulliver, Quantum field lens coding and classification algorithm to predict measurement outcomes, *MethodsX* 10 (2023) 102136, doi:[10.1016/j.mex.2023.102136](https://doi.org/10.1016/j.mex.2023.102136).
- [8] P.B. Alipour, T.A. Gulliver, A double-field computation model to simulate physical systems, *Comp. SciRN Elsev. e-J., Comp. Theo* 6 (2023) 10, doi:[10.2139/ssrn.4239321](https://doi.org/10.2139/ssrn.4239321).
- [9] P.B. Alipour, T.A. Gulliver, Quantum double-field model and application, preprint via PHYSO-EM, Elsevier. e-J. 4233203 (2022) 28, doi:[10.2139/ssrn.4233203](https://doi.org/10.2139/ssrn.4233203).
- [10] P.B. Alipour, T.A. Gulliver, Dataset for quantum double-field model and application, Mendeley Data, Elsevier BV, 2022 V2+ <https://data.mendeley.com/datasets/gf2s8jkdjf>.
- [11] P.B. Alipour, T.A. Gulliver, QF-LCA dataset: Quantum field lens coding algorithm for system state simulation and strong predictions. To appear on Data-in-Brief, Elsevier BV, 2023 or see review submission at Mendeley Data, Elsevier BV (2023) V3+ <https://data.mendeley.com/datasets/gf2s8jkdjf>.
- [12] N.L. Hegade, N.L. Kortikar, B. Das, B.K. Behera, P.K. Panigrahi, Experimental demonstration of multi-particle quantum tunneling on IBM quantum computer, (quant-ph) arXiv.org, 2021. <https://doi.org/10.48550/arXiv.1712.07326>.
- [13] B. Nachman, D. Provasoli, W.A. de Jong, C.W. Bauer, Quantum algorithm for high energy physics simulations, *Phys. Rev. Lett.* 126 (2021) 062001, doi:[10.1103/PhysRevLett.126.062001](https://doi.org/10.1103/PhysRevLett.126.062001).
- [14] D. Bachtis, G. Aarts, F.D. Renzo, B. Lucini, Inverse renormalization group in QFT, *Phys. Rev. Lett.* 128 (2022) 081603, doi:[10.1103/PhysRevLett.128.081603](https://doi.org/10.1103/PhysRevLett.128.081603).
- [15] J. Liu, Ph.D. dissertation, R. Does, Feynman dream of electric sheep? Topics on QFT, quantum computing and computer science, Caltech (2021) <https://thesis.library.caltech.edu/14142>.
- [16] J. Liu, Y. Xin, Quantum simulation of quantum field theories as quantum chemistry, *High Ener. Phys. J.*, SpringerLink (2020) 11 10.1007/JHEP12(2020)011; image extracts from the preprint at, doi:[10.48550/arXiv.2004.13234](https://doi.org/10.48550/arXiv.2004.13234).
- [17] K. Yeter-Aydeniz, E. Moschandreas, G. Siopsis, Quantum Imaginary-time evolution algorithm for quantum field theories with continuous variables, *Phys. Rev. A* 105 (2022) 012412 <https://journals.aps.org/prx/abstract/10.1103/PhysRevA.105.012412>.
- [18] M. Bagherinehrab, Y.R. Sanders, D.W. Berry, G.K. Brennen, B.C. Sanders, Nearly optimal quantum algorithm for generating the ground state of a free quantum field theory, *PRX Quant.* 3 (2022) 020364, doi:[10.1103/PRXQuantum.3.020364](https://doi.org/10.1103/PRXQuantum.3.020364).
- [19] S. Abel, N. Chancellor, M. Spannowsky, Quantum computing for quantum tunneling, *Phys. Rev. D* 103 (2021) 016008, doi:[10.1103/PhysRevD.103.016008](https://doi.org/10.1103/PhysRevD.103.016008).
- [20] V. Wadhia, M.Sc. Thesis, Quantum Field Theory Simulation using Digital Quantum Computers, Durham University, UK, 2021 <http://etheses.dur.ac.uk/14306/>.
- [21] I. Hobday, P.D. Stevenson, J. Benstead, Quantum computing calculations for nuclear structure and nuclear data, in: Proc. SPIE, Quant. Tech. 12133, 2022, doi:[10.1117/12.2632782](https://doi.org/10.1117/12.2632782).
- [22] R. Miceli, M. McGuigan, Quantum computation and visualization of Hamiltonians using discrete quantum mechanics and IBM Qiskit, in: New York Scientific Data Summit, IEEE, NY, USA, 2018, pp. 1–6. <https://ieeexplore.ieee.org/document/8538959>.
- [23] C. Allende, A.F. de Oliveira, E. Baksman, Characterizing errors for quantum Fourier transform on IBM, Q, *Rev. Mex. Fís.* 68 (2022) 3, doi:[10.31349/RevMexFis.68.031402](https://doi.org/10.31349/RevMexFis.68.031402).
- [24] S. Shokri, S. Rafibakhsh, R. Pooshgan, R. Faeghi, Implementation of a quantum algorithm to estimate the energy of a particle in a finite square well potential on IBM quantum computer, *Euro. Phys. J. Plus* 136 (2021) 762, doi:[10.1140/epjp/s13360-021-01743-y](https://doi.org/10.1140/epjp/s13360-021-01743-y).
- [25] T. Giamarchi, C. Rüegg, O. Tchernyshyov, Bose-Einstein condensation in magnetic insulators, *Nat. New.* (2008) <https://www.nature.com/articles/nphys893>. [accessed Feb. 5, 2023].
- [26] J. Stolze, D. Suter, *Quantum Computing*, 1st ed., Wiley-VCH, 2004 1–62, 217, Chaps. 1, 2, 4, 6–8, 10–13.
- [27] R.P. Feynman, Simulating physics with computers, *Int. J. Theor. Phys.* 21 (1982) 467–488, doi:[10.1007/BF02650179](https://doi.org/10.1007/BF02650179).
- [28] J. Preskill, Simulating quantum field theory with a quantum computer, (hep-lat) arXiv.org, 2018. <https://doi.org/10.48550/arXiv.1811.10085>.
- [29] N.M.P. Neumann, Classification using a two-qubit quantum chip, in: *Comput. Sci. ICCS* 2021. Lecture Notes in Computer Science, Springer, 2021, p. 12747, doi:[10.1007/978-3-030-77980-1_6](https://doi.org/10.1007/978-3-030-77980-1_6).
- [30] R. Wezeman, N. Neumann, F. Phillipson, Distance-based classifier on QInspire at Springer, *Digit. Welt* 4 (2020) 85–91, doi:[10.1007/s42354-019-0240-5](https://doi.org/10.1007/s42354-019-0240-5).
- [31] A. C-Lierta, J.S. Kottmann, Aln A-Guzik, Meta-variational quantum eigen solver: learning energy profiles of parameterized Hamiltonians for quantum simulation, *Phys. Rev. X Quant.* 2 (2021) 020329, doi:[10.1103/PRXQuantum.2.020329](https://doi.org/10.1103/PRXQuantum.2.020329).
- [32] C.M. Van Vliet, in: *Equilibrium and Nonequilibrium Statistical Thermodynamics*, WSP, 2010, pp. 5–42. 127–163.
- [33] IBM-QE, A quantum computing platform as a Circuit Composer at <https://quantum-computing.ibm.com/composer/docs/iqx/guide/introducing-qubit-phase>; Quantum phase (shift) gates, QFT and superdense coding from <https://quantum-computing.ibm.com/jupyter/user/qiskit-textbook/content/ch-algorithms/superdense-coding.ipynbaQiskitnotebook> [accessed 2022].
- [34] M. Sadri, Persiphila Philatelic Reference (c. 1865–1896) (Persiphila books, CA USA 2020) pp. 93–96. <https://www.persi.com/booksandalbums/index.html>. Also, see Classic stamp forgeries: Persian lion 1868 (2021), at <https://stampforgeries.blogspot.com/2021/01/iran-lion-issue.html> [accessed Feb. 2023].
- [35] D. Feldman, 1878 Persian lion stamp, Type D, sold from the authenticated used set of 32K USD, as Los 10307 - 1878-79 One Toman bronze red on thin blue porous paper, Dec. 2020 Auction Series at https://www.davidfeldman.com/de/dfsa-auktionen/2020-december-auction-series/persia-dec-2020/1878-79-re-engraved-sg-37-39-persiphila-26-28-one/?soft_session_page=4&soft_auction_browse=1, or, Persia, Including the Khosrow “Joe” Youssefi Collection (Part 2), Nov. 30, 2020, Geneva (David Feldman SA), p. 99 (2020), source file at https://dsy73arn0qite.cloudfront.net/2020/11/Stamp_auction_catalogue_Persia_Dec2020.pdf. Also, Philasearch auction on the catalogue value from https://www.philasearch.com/en/i_9369_35936/3330_Persia_Iran/9369-A95-644.html?treeparent=COSUBGRP-31200&set_sprache=en&locale=en&postype=result&row_nr=8&breadcrumbId=1677840208.2936 [accessed Feb. 2023].
- [36] K. Muldoon, Y. Song, Z. Ahmad, X. Chen, M-W. Chang, High precision 3D printing for micro to nano-scale biomedical and electronic devices, *Micromachines* 13 (4) (2022) 642, doi:[10.3390/mi13040642](https://doi.org/10.3390/mi13040642).
- [37] D.M. Tran, V-D. Nguyen, L.B. Ho, H.Q. Nguyen, Increased success probability in Hardy’s nonlocality: theory and demonstration, *Phys. Rev. A* 107 (4) (2023) 042210, doi:[10.1103/PhysRevA.107.042210](https://doi.org/10.1103/PhysRevA.107.042210).
- [38] J-M. Liang, Q-Q. Lv, Z-X. Wang, S-M. Fei, Assisted quantum simulation of open quantum systems, *iScience* 26 (4) (2023) 106306, doi:[10.1016/j.isci.2023.106306](https://doi.org/10.1016/j.isci.2023.106306).
- [39] P. Hyllus, Fisher information and multiparticle entanglement, *Phys. Rev. A* 85 (2012) 022321, doi:[10.1103/PhysRevA.85.022321](https://doi.org/10.1103/PhysRevA.85.022321).
- [40] P. Hauke, L. Bonnes, M. Heyl, W. Lechner, Probing entanglement in adiabatic quantum optimization with trapped ions, *Front. Phys.* 3 (2015) 21, doi:[10.3389/fphy.2015.00021](https://doi.org/10.3389/fphy.2015.00021).
- [41] I.B. Djordjevic, Quantum Communication, Quantum Networks and Quantum Sensing, Acad. Press, 2023 Chap. 12, doi:[10.1016/B978-0-12-822942-2.00010-8](https://doi.org/10.1016/B978-0-12-822942-2.00010-8).
- [42] J. Daragan, Top 63 Quantum computer simulators For 2022 from the quantum inspired, at <https://thequantuminsider.com/2022/06/14/top-63-quantum-computer-simulators-for-2022>. Selected simulator is No. 27: Q-Kit from 2020. [accessed Jun 2023].

- [43] A. Tankasala, H. Ilatikhamenehquant-ph arXiv.org, Quantum-Kit: Simulating Shor's Factorization of 24-Bit Number on Desktop, 2020. <https://arxiv.org/abs/1908.07187>.
- [44] T. Suzuki, T. Miyazaki, T. Inaritai, et al., Quantum AI simulator using a hybrid CPU-FPGA approach, *Sci. Rep.* 13 (2023) 7735, doi:[10.1038/s41598-023-34600-2](https://doi.org/10.1038/s41598-023-34600-2).
- [45] B.J. MacLennan, in: *Quantum Inspired Computational Intelligence*, Morgan Kaufmann, 2017, pp. 85–110, doi:[10.1016/B978-0-12-804409-4.00003-6](https://doi.org/10.1016/B978-0-12-804409-4.00003-6). Chap. 3.
- [46] P. Migdał, K. Jankiewicz, P. Grabarz, C. Decaroli, P. Cochin, Visualizing quantum mechanics in an interactive simulation – virtual lab by quantum flytrap, *Opt. Eng.* 61 (8) (2022) 081808, doi:[10.1117/1.OE.61.8.081808](https://doi.org/10.1117/1.OE.61.8.081808).
- [47] X. Zhao, A. Ilderton, P. Maris, J.P. Vary, Scattering in time-dependent basis light-front quantization, *Phys. Rev. D* 88 (2013) 065014, doi:[10.1103/PhysRevD.88.065014](https://doi.org/10.1103/PhysRevD.88.065014).
- [48] CERN Open Data Portal, QFT datasets to simulate from CERN at <https://opendata.cern.ch/>, try e.g. <https://opendata.cern.ch/search?page=1&size=20&type=Dataset> with data access levels by LHC available at <https://opendata.cern.ch/docs/about> [accessed Jun 2023].
- [49] N. Khammasi (developer), QX Simulator, to simulate a run on a quantum computer by QuTech QX-26, 31, 34-L simulators, or quantum processors as Spin-4 and Stramon-5 to run at [https://www.quantum-inspire.com/backends/qx-simulator/\(quantum-inspire.com\)](https://www.quantum-inspire.com/backends/qx-simulator/(quantum-inspire.com)) [accessed, 2020-2023].
- [50] QInspire, The multi-hardware Quantum Technology platform, Quant. inspire platform, TU Delft Univ., NE, at <https://www.quantum-inspire.com/> [accessed, 2020-2023].
- [51] J. Renema (University of Twente AQOpt Research Group), Time reversal photonics experiment resolves quantum paradox, a short illustrative report at <https://scitechdaily.com/time-reversal-photonics-experiment-resolves-quantum-paradox/> [accessed Jul 9, 2023].
- [52] F.H.B. Somhorst, R. van der Meer, M.C. Anguita, et al., Quantum simulation of thermodynamics in an integrated quantum photonic processor, *Nat. Commun.* 14 (2023) 3895, doi:[10.1038/s41467-023-38413-9](https://doi.org/10.1038/s41467-023-38413-9).
- [53] S. Leontica, F. Tennie, T. Farrow, Simulating molecules on a cloud-based 5-qubit IBM-Q universal quantum computer, *Commun. Phys.* 4 (2021) 112, doi:[10.1038/s42005-021-00616-1](https://doi.org/10.1038/s42005-021-00616-1).
- [54] F. Tacchino, A. Chiesa, S. Carretta, D. Gerace, Quantum computers as universal quantum simulators: state-of-the-art and perspectives, *Adv. Quant. Tech.* 3 (2020) 1900052, doi:[10.1002/qute.201900052](https://doi.org/10.1002/qute.201900052).
- [55] I. Navabshan, B. Sakthivel, R. Pandiyan, et al., Computational lock and key and dynamic trajectory analysis of natural biophors against COVID-19 spike protein to identify effective lead molecules, *Mol. Biotech.* 63 (2021) 898–908, doi:[10.1007/s12033-021-00358-z](https://doi.org/10.1007/s12033-021-00358-z).
- [56] S.K. Kundu, A. Pradhan, C. Rosenzweig, Does the vacuum gravitate on microscopic scales? rydberg atoms indicate probably not (hep-th), arXiv.org. (2023), [10.48550/arXiv.2208.14192](https://arxiv.org/abs/2208.14192).
- [57] S.K. Jagatheesaperumal, M. Rahouti, K. Ahmad, A. Al-Fuqaha, M. Guizani, The duo of artificial intelligence and big data for industry 4.0: applications, techniques, challenges, and future research directions, *IEEE Internet of Thing. J.* 9 (2022) 15, doi:[10.1109/JIOT.2021.3139827](https://doi.org/10.1109/JIOT.2021.3139827).
- [58] H. Liu, A.S. Helmy, Joint measurement of time-frequency entanglement via sum frequency generation, *npj Quant. Inf.* 6 (2020) 66, doi:[10.1038/s41534-020-00293-y](https://doi.org/10.1038/s41534-020-00293-y).
- [59] S. Yarkoni, et al., Quantum annealing for industry applications: introduction and review, *Rep. Prog. Phys.* 85 (2022) 104001, doi:[10.1088/1361-6633/ac8c54](https://doi.org/10.1088/1361-6633/ac8c54).
- [60] X. Qiu, P. Zoller, X. Li, Programmable quantum annealing architectures with Ising quantum wires, *PRX Quant.* 1 (2020) 020311, doi:[10.1103/PRXQuantum.1.020311](https://doi.org/10.1103/PRXQuantum.1.020311).